# Electronic Supplementary Information (ESI)

## Fluorinated 2D conjugated porous organic polymer films with modular structural topology for controlled molecular sieving

*Jessica Gayle[1,#], Rifan Hardian[2,#], Galio Guo[1], Xu Wang[3], Muhammad M. Rahman[1], Rafael Verduzco[1,4], Robert Vajtai[1], Pulickel Ajayan[1*], Soumyabrata Roy[1*], Gyorgy Szekely[2,5*]*

[1]Department of Materials Science and NanoEngineering, Rice University, Houston, Texas 77005, United States.

[2]Advanced Membranes and Porous Materials Center, Physical Science and Engineering Division, King Abdullah University of Science and Technology (KAUST), Thuwal 23955-6900, Saudi Arabia.

[3]Shared Equipment Authority, Rice University, Houston, Texas, United States.

[4]Department of Chemical and Biomolecular Engineering, Rice University, Houston, Texas 77005, United States.

[5]Chemical Engineering Program, Physical Science and Engineering Division (PSE), King Abdullah University of Science and Technology (KAUST), Thuwal, 23955-6900, Saudi Arabia

[#]These authors contributed equally.

[*]Corresponding author. Email: ajayan@rice.edu; s.roy@rice.edu; gyorgy.szekely@kaust.edu.sa

**Contents**

**List of Table**



**List of Figures**

# 1. **Materials and Methods**

## *1.1. Materials*

Solvents including, dioxane, hexane, acetone, and methanol were purchased from MilliporeSigma. 1,3,5-tris(4-aminophenyl)benzene (**TAPB**) and terephthalaldehyde (**TP**) were purchased from TCI chemicals. 2,3,5,6-tetrafluoroterephthalaldehyde (**Tf**), 4,4',4''-triaminotriphenylamine (**TAPA**), 5,5',5''-(1,3,5-triazine-2,4,6-tryl)trianiline)(**TZ**), 4,4',4'',4'''-(ethene-1,1,2,2-tetrayl)tetraaniline (**ETTA**) was purchased from Ambeed. All materials were used as received with our further modification. Toluene (≥99.5%), acetone (≥99.5%), acetonitrile (≥99.5%), methanol (≥99.5%), and hexane (≥99.5%) were purchased from Sigma-Aldrich. The markers for the nanofiltration experiment, namely styrene dimer (236.35 g $mol^{-1}$), methyl orange (327.33 g $mol^{-1}$), losartan (422.92 g $mol^{-1}$), 4CzIPN (788.89 g $mol^{-1}$), roxithromycin (837.06 g $mol^{-1}$), rose bengal (973.67 g $mol^{-1}$), Ir-complex CAS 870987-63-6 (1121.91 g $mol^{-1}$), and Ru-complex CAS 75777-87-6 (1196. 19 g $mol^{-1}$) were also obtained from Sigma Aldrich. All the materials were used as received without further modification.

## *1.2. Instrumentation*

**Profilometer:** Bruker DEKTAK Stylus Profilometer was used to obtain height mapping of bulk films deposited on glass. Thickness was measured for films using different monomer concentrations.

**Fourier transform infrared (FTIR):** Nicolet iS50 spectrometer was with a KBr detector with Smart iTX-Accessory with diamond crystal was used to obtain %Transmittance measurements.

**SS-$^{13}$CNMR:** 4.7 T (50.3 MHz $^{13}$C and 200.1 MHz 1H) Brucker spectrometer was used with 2 ms contact time and 7.6 kHz MAS and 5 s relaxation delay after 32.8 ms FID was performed.

**Brunauer–Emmett–Teller (BET):** Quantachrome Autosorb-iQ3-MP/Kr BET surface analyzer was used to characterize film pieces. Films were outgassed at 120 °C for 12 hours. For $N_2$ and $CO_2$ measurements 67 adsorption and 40 desorption points were used. NLDFT model was used on $N_2$ isotherms to obtain pore size distribution.

.

**X-ray diffraction (XRD):** Rigaku Smartlab XE diffractometer with Cu Ka X-ray tube was used. For PXRD measurements, sonicated film pieces were placed on a zero-background holder and characterized using parallel beam from 1-40° two theta at a scan rate of 2 °C $min^{-1}$. For 2D WAXS measurements, bulk films were cut into small film strips and the film cross-section was aligned to x-ray beam and detector**.**

**Scanning electron microscopy (SEM):** FEI Helios NanoLab 660 Dual Beam SEM was used to image bulk films and cross sections in addition to exfoliated film flakes to see layered structure as film fracture edge.

**Contact Angle:** Ramé-Hart Model 250 Contact angle Goniometer was used to measure the water contact angle on pristine films that were dried overnight at 50 °C vacuum.

**Polarizing Optical Microscope:** Zeiss Axioplan II microscope with an Axiocam 208 color camera was used to image exfoliated films nanosheets on glass using transmission mode.

**Atomic force microscopy (AFM):** AFM NX20 Microscope with Brucker TESPA-V2 antimony-doped silicon probes tips were used to characterize the thickness of exfoliated film flakes using non-contact mode.

**Thermogravimetric analysis (TGA):** Mettler Toledo TGA/DSC 3+ system was used to measure thermostability of film pieces with a ramp rate of 5 °C $min^{-1}$ to 100 °C stabilized for 15 minutes then a ramp rate of 5 °C $min^{-1}$ to 1000 °C all with a $N_2$ flow rate at 100 mL $min^{-1}$.

**Nanoindentation:** Hysitron TI 980 Triboindentor was used to perform displacement-controlled indentions with a load rate of 25 nm $s^{-1}$ and hold time of 2 seconds.

# 2. Synthesis and materials characterizations

## *2.1. Film Synthesis*

Fluorinated films were synthesized through condensation reactions between bi-functional aldehyde monomer Tf with either tri-(TAPB, TAPA,TZ) or tetra-functionalized (ETTA) amine monomers. To form TAPB–Tf, TAPA–Tf, and TZ–Tf films, 0.0317 mmol of TAPB, TAPA, or TZ was dissolved with 0.0476 mmol Tf in 1.5 mL of dioxane to form a dilute precursor solution. For ETTA–Tf film, the same method was modified to adjust for proper molar ratios using 0.0264 mmol ETTA and 0.0528 mmol for Tf. Synthesis of non-fluorinated films (–TP) followed the previously reported method.[1]

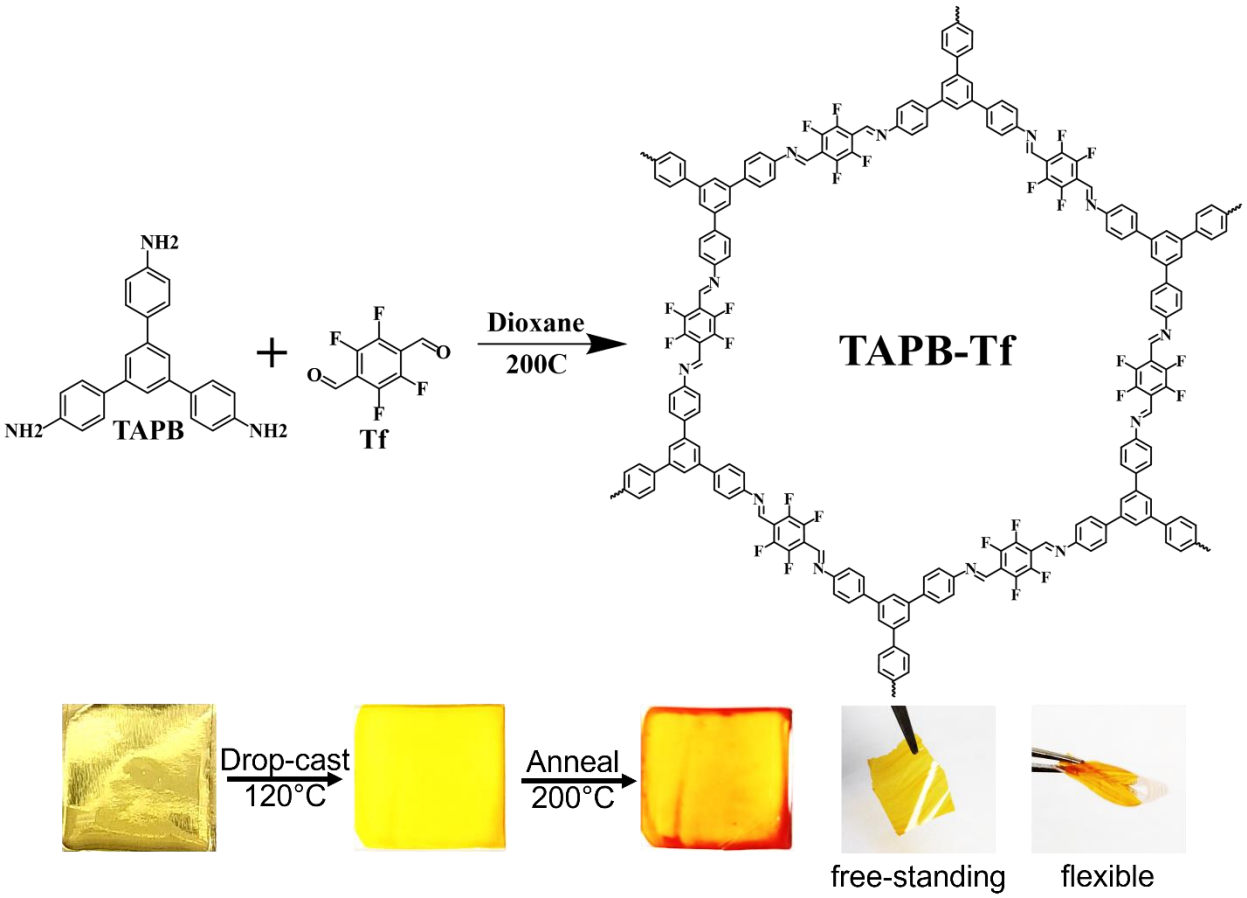


**Figure S1.** Reaction scheme for TAPB–Tf film produced from polymerization of TAPB and Tf starting monomers. Films produced were free-standing and flexible.

**TAPB–Tf film:** 11.14 mg (0.0317 mmol, MW= 351.44 g $mol^{-1}$) TAPB + 9.81 mg (0.0476 mmol, MW= 206.09 g $mol^{-1}$) Tf, and 2 mL of dioxane was added to 4 mL scintillation vial.

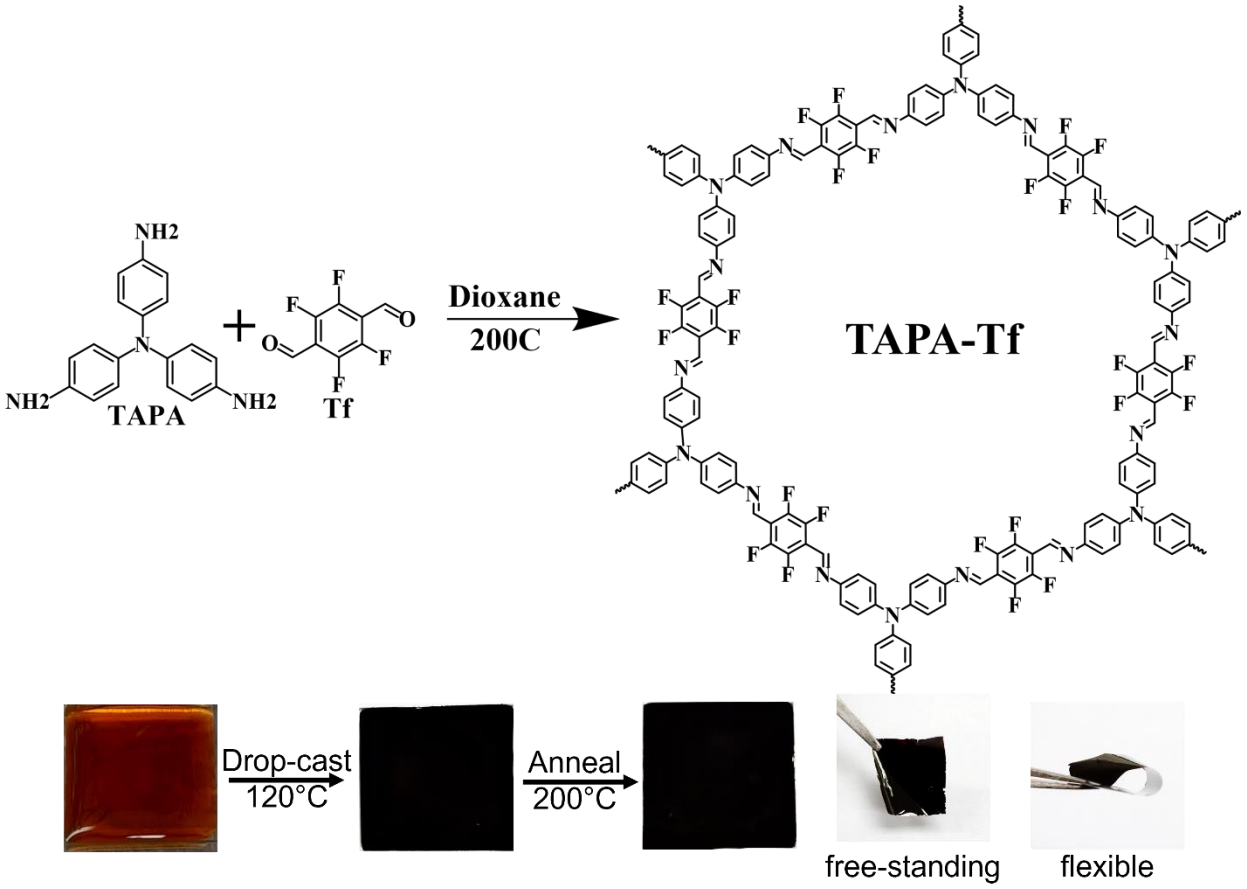


**Figure S2.** Reaction scheme for TAPA–Tf film produced from polymerization of TAPA and Tf starting monomers. Films produced were free-standing and flexible.

**TAPA–Tf film:** 9.20 mg (0.0317 mmol, MW= 290.36 g $mol^{-1}$) TAPB + 9.81 mg (0.0476 mmol, MW= 206.09 g $mol^{-1}$) Tf, and 2 mL of dioxane was added to 4 mL scintillation vial.

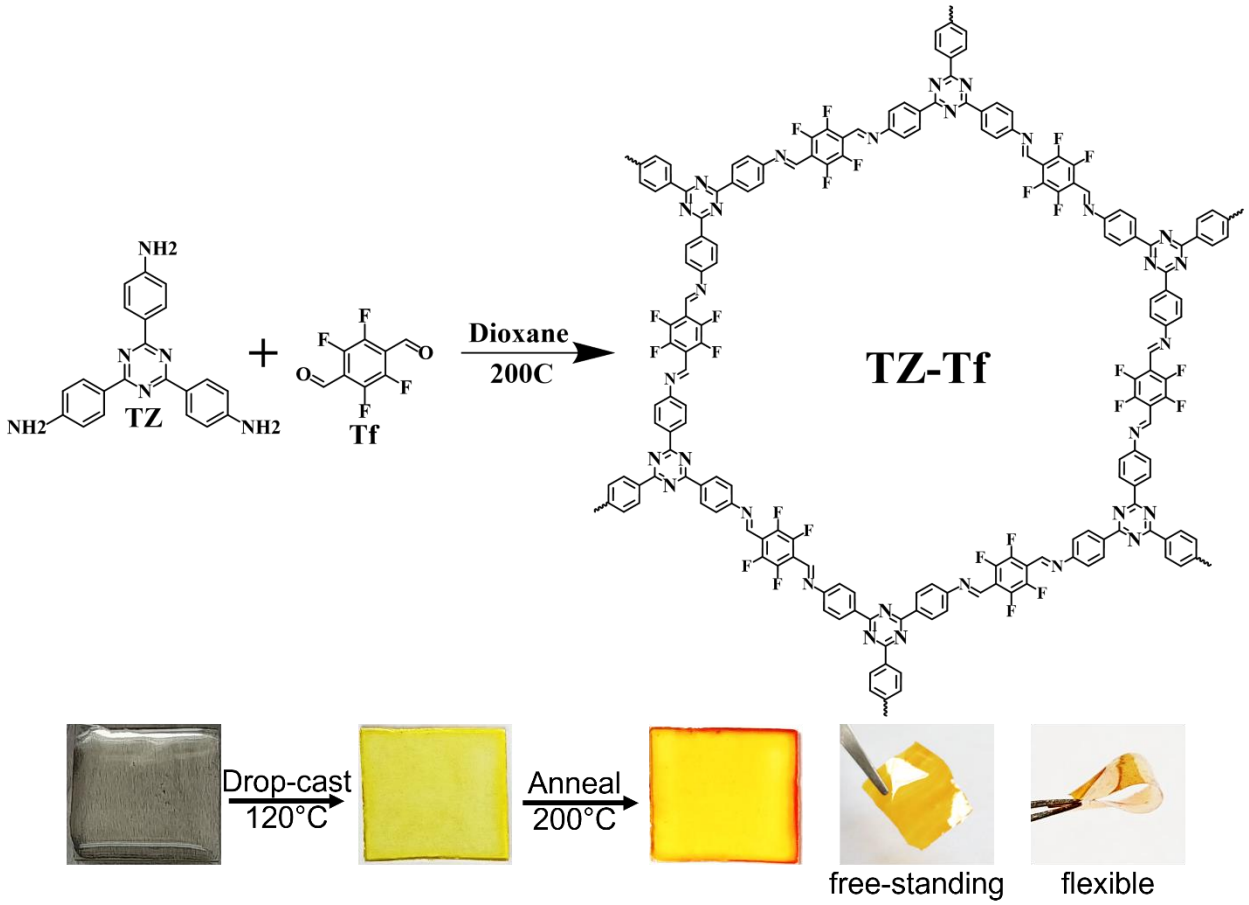


**Figure S3.** Reaction scheme for TZ–Tf film produced from polymerization of TZ and Tf starting monomers. Films produced were free-standing and flexible.

**TZ–Tf film:** 11.24 mg (0.0317 mmol, MW= 354.41 g $mol^{-1}$) TZ + 9.81 mg (0.0476 mmol, MW= 206.09 g $mol^{-1}$) Tf, and 2 mL of dioxane was added to 4 mL scintillation vial.

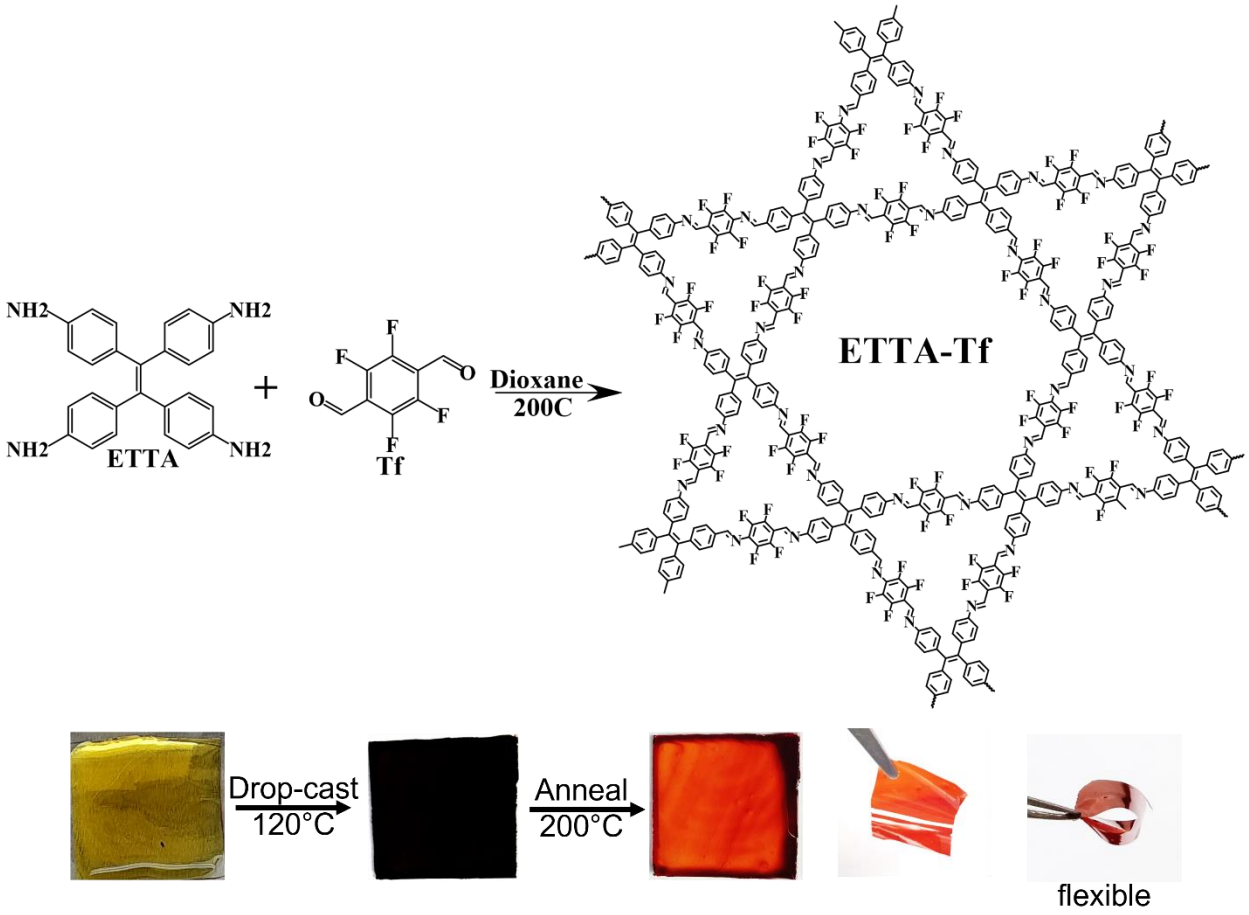


**Figure S4.** Reaction scheme for ETTA–Tf film produced from polymerization of ETTA and Tf starting monomers. Films produced were free-standing and flexible.

**ETTA–Tf film:** 10.37 mg (0.0264 mmol, MW= 392.50 g $mol^{-1}$) ETTA + 10.88 mg (0.0528 mmol, MW= 206.09 g $mol^{-1}$) Tf, and 2 mL of dioxane was added to 4 mL scintillation vial.

**Drop-casted Films**: The precursor solutions with starting monomers and solvent were deposited onto glass substrates and heated on the hotplate for 30 minutes at 120 °C. After 10 minutes full evaporation of solvent and film formation was observed. Films were then annealed for 12 hours under vacuum at 200 °C for 12 hours.

**Exfoliated Films:** Films were exfoliated by breaking large film pieces into a small vial filled with dioxane. This solution was then frozen, thawed, and then sonicated for 1 hour. This was repeated 3 times. Large film pieces were allowed to settle for 30 minutes and the smaller pieces in the top solution layer was used for further characterization and analysis.

*2.1. Film characterizations*

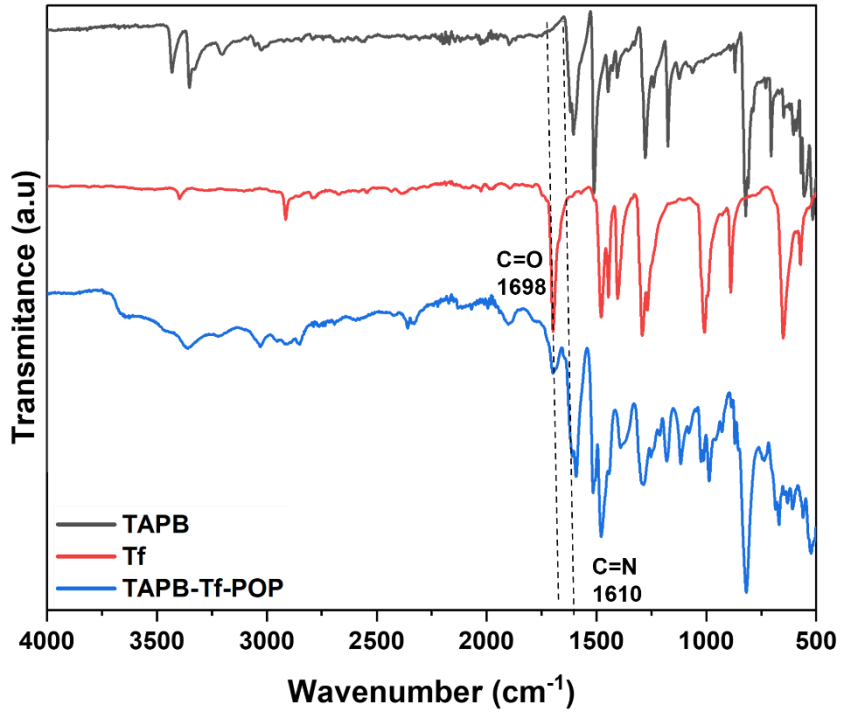


**Figure S5.** FTIR of TAPB–Tf film showing formation of imine bond from starting materials.

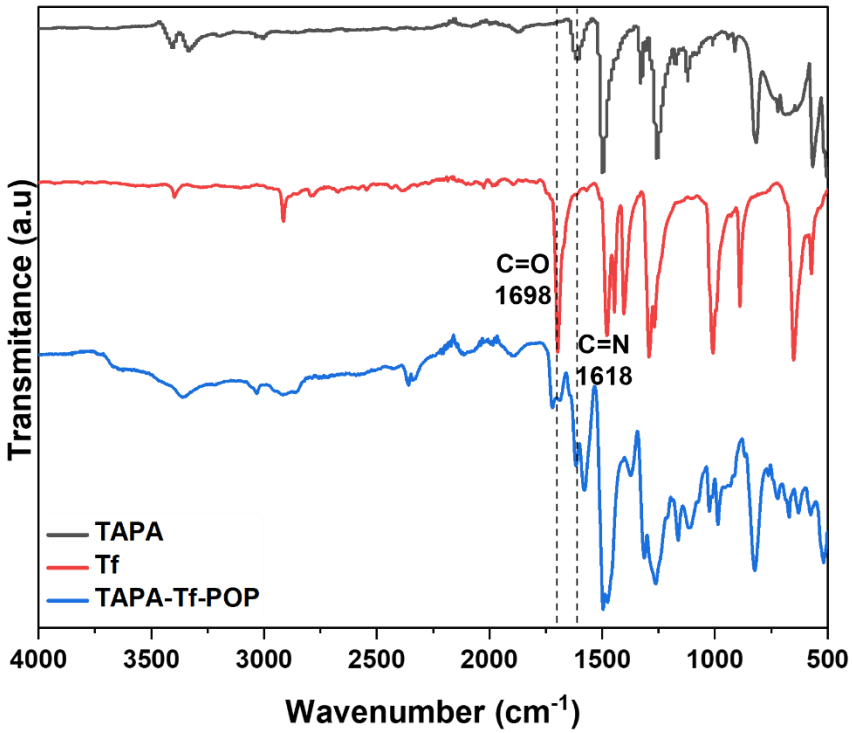


**Figure S6.** FTIR of TAPA–Tf film showing formation of imine bond from starting materials.

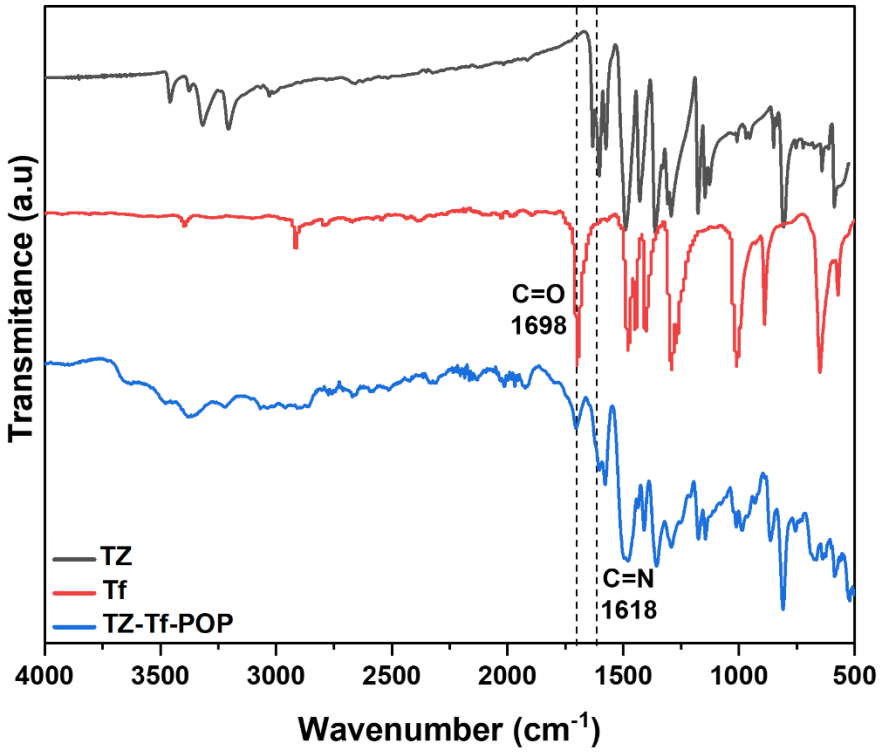


**Figure S7.** FTIR of TZ–Tf film showing formation of imine bond from starting materials.

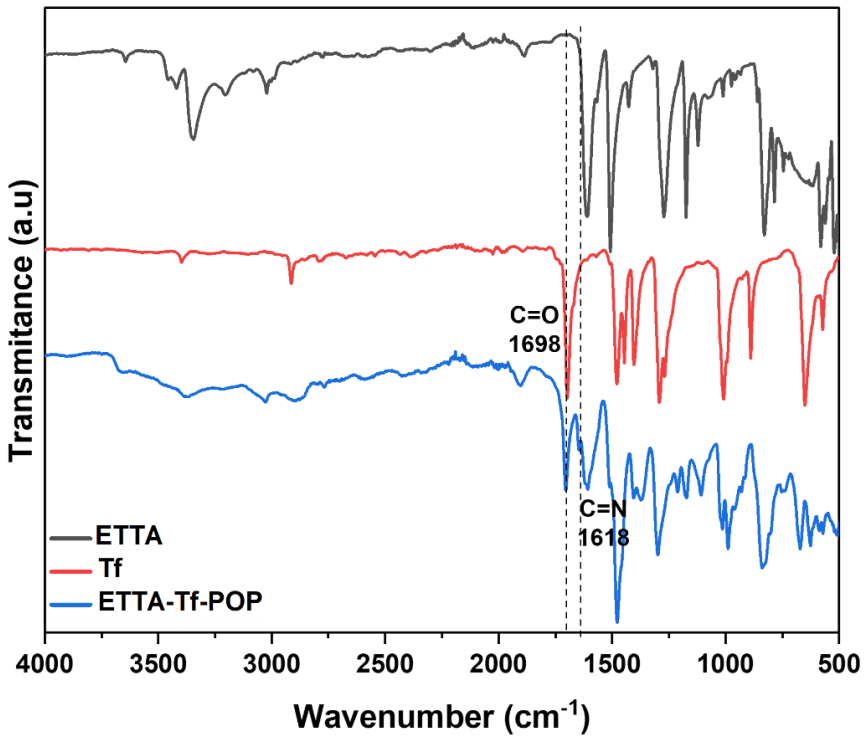


**Figure S8.** FTIR of ETTA–Tf film showing formation of imine bond from starting materials.

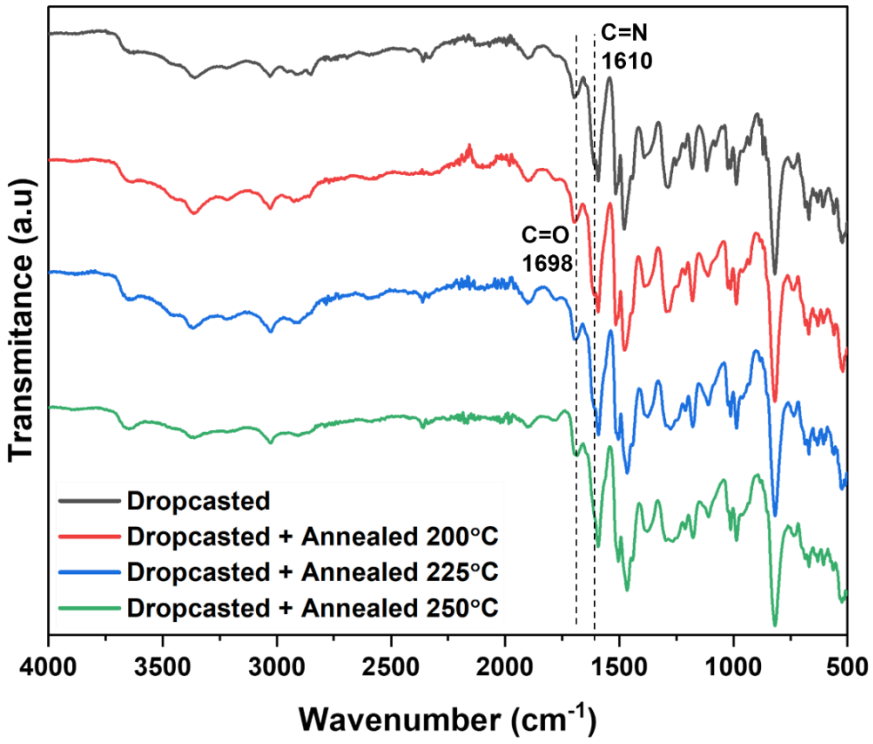


**Figure S9.** FTIR of TAPB–Tf film when annealed at varied temperatures 200 °C-250 °C for 12 hours showing changes in relative intensity of imine to aldehyde peak.

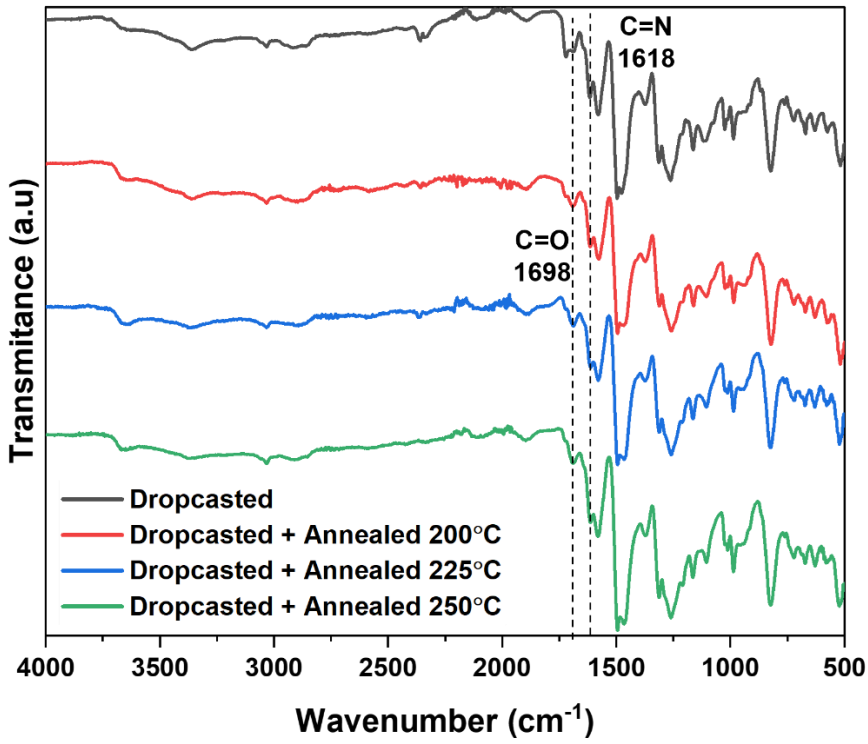

**Figure S10.** FTIR of TAPA–Tf film when annealed at varied temperatures 200 °C-250 °C for 12 hours showing changes in relative intensity of imine to aldehyde peak.

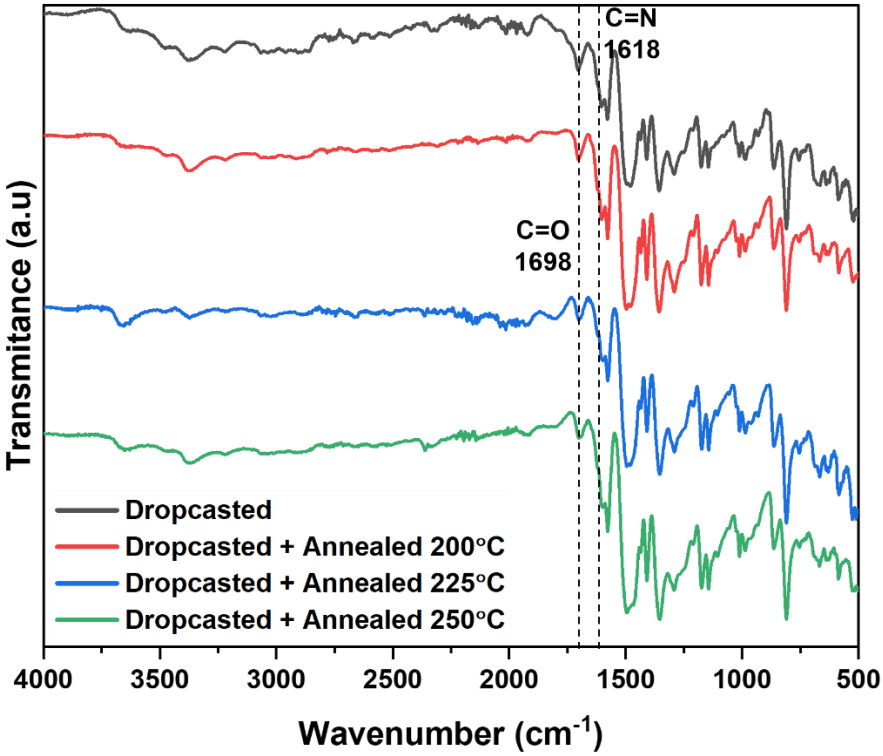


**Figure S11.** FTIR of TZ–Tf film when annealed at varied temperatures 200 °C-250 °C for 12 hours showing changes in relative intensity of imine to aldehyde peak.

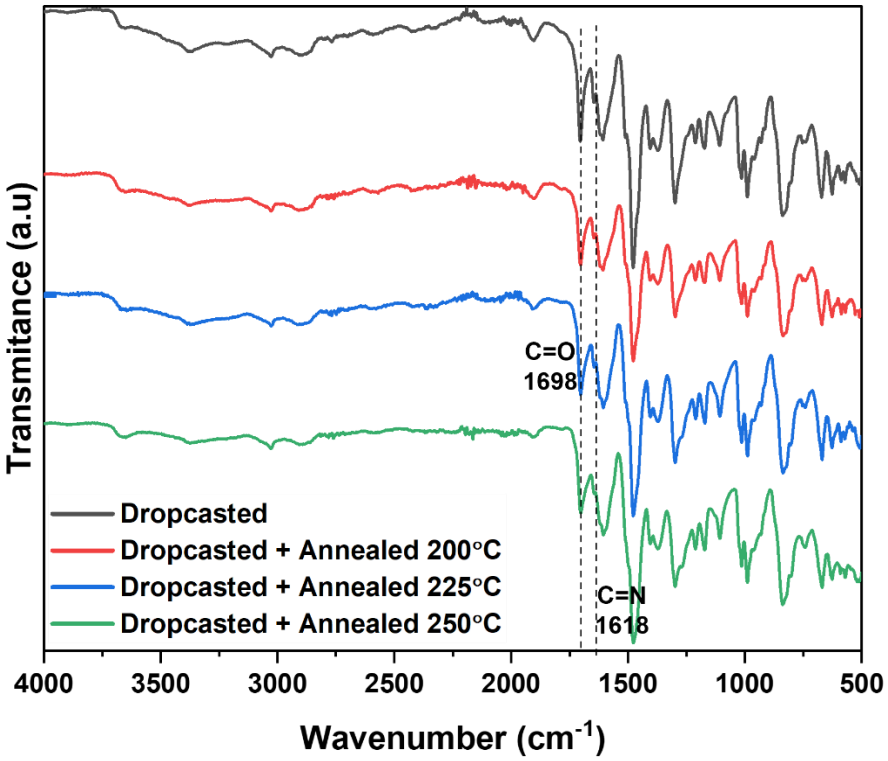


**Figure S12.** FTIR of ETTA–Tf film when annealed at varied temperatures 200 °C-250 °C for 12 hours showing changes in relative intensity of imine to aldehyde peak.

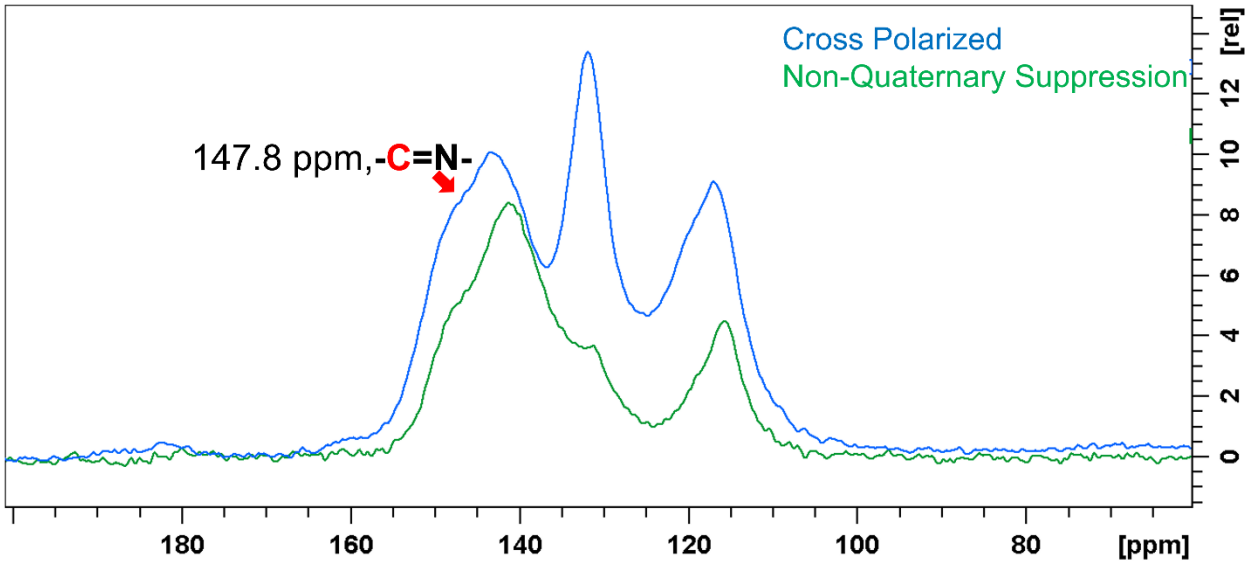


**Figure S13.** SS-$^{13}$CNMR cross-polarized and non-quaternary suppression was performed on TAPB–Tf film.

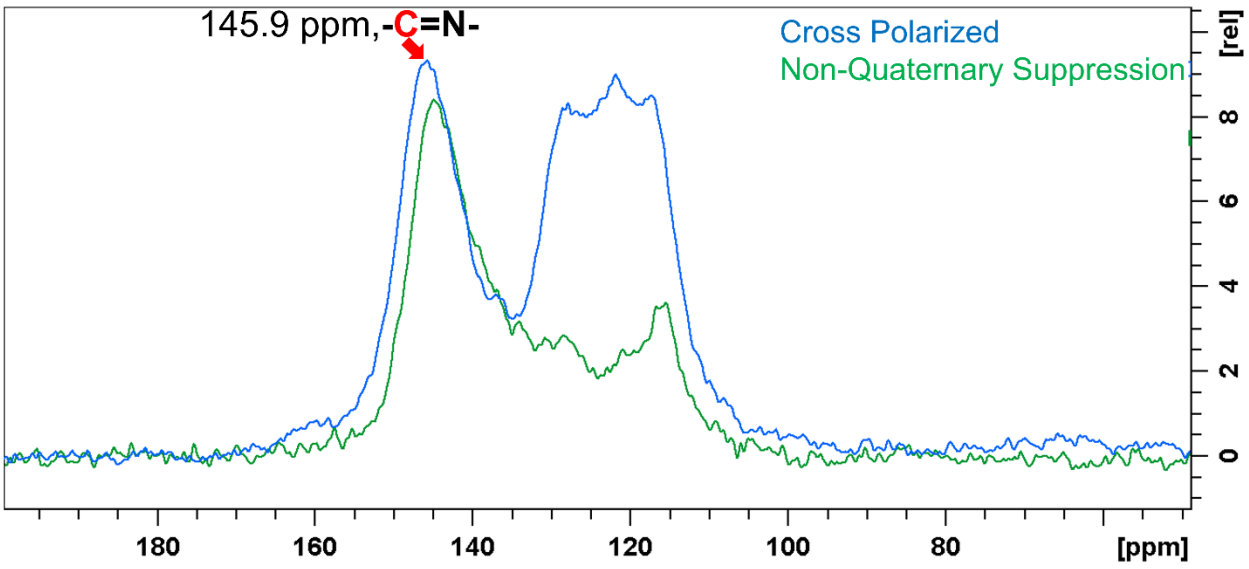


**Figure S14.** SS-$^{13}$CNMR cross-polarized and non-quaternary suppression was performed on TAPA–Tf film.

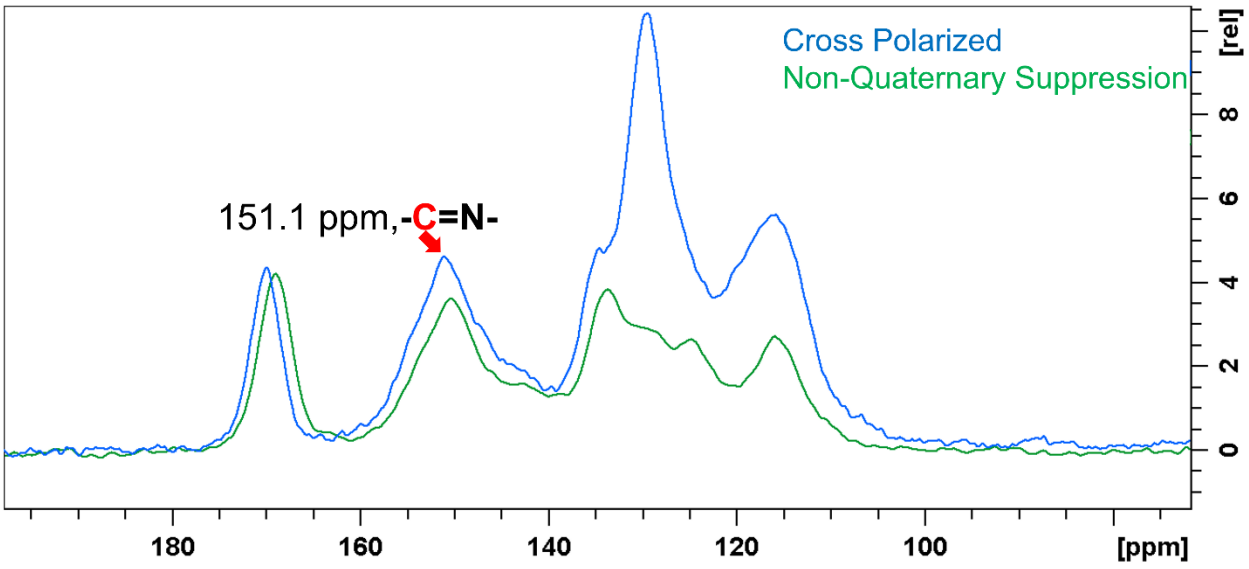


**Figure S15.** SS-$^{13}$CNMR cross-polarized and non-quaternary suppression was performed on TZ–Tf film.

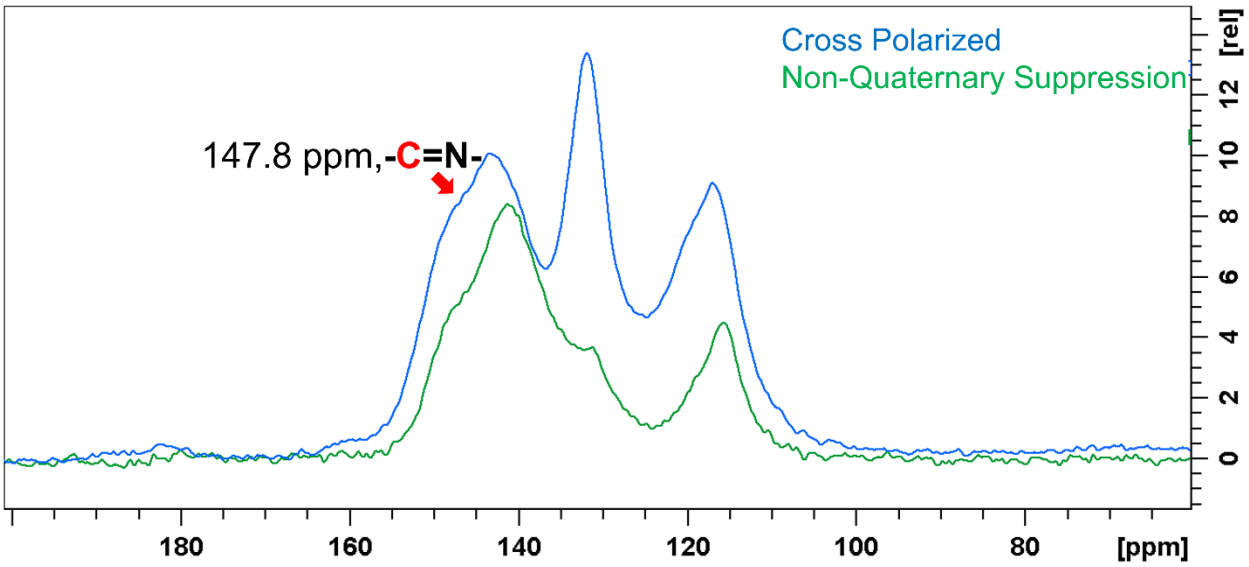


**Figure S16.** SS-$^{13}$CNMR cross-polarized and non-quaternary suppression was performed on ETTA–Tf film.

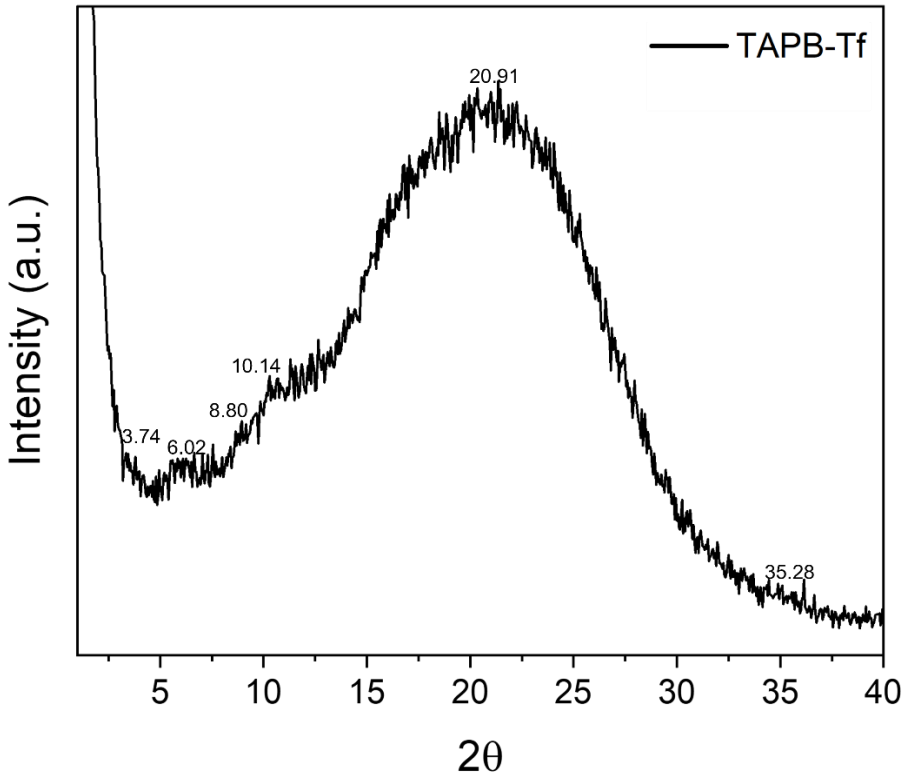


**Figure S17.** PXRD pattern of TAPB–Tf film.

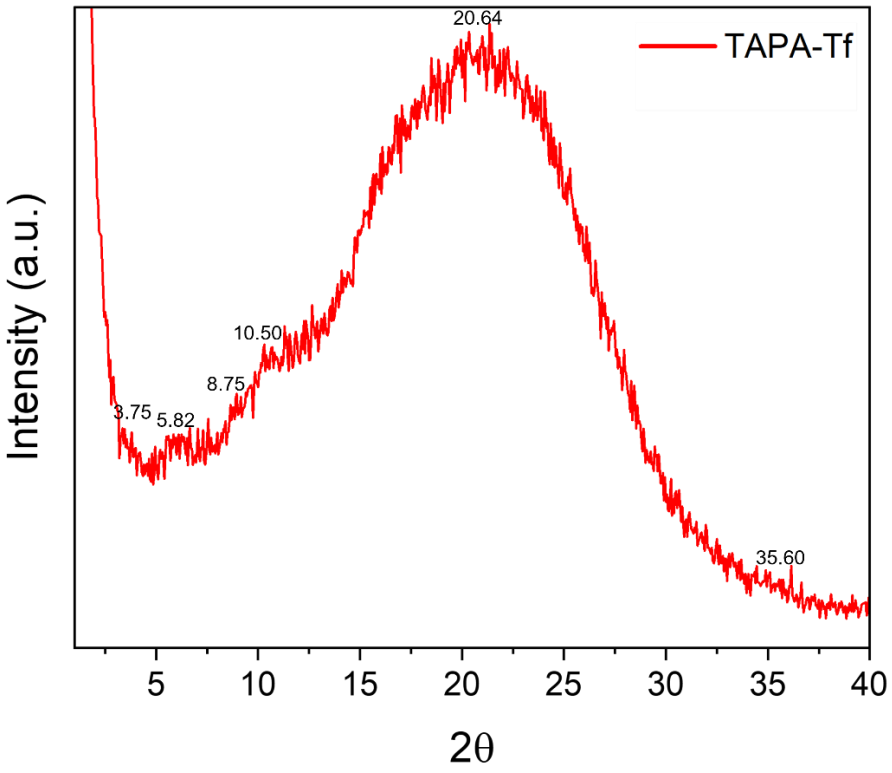


**Figure S18.** PXRD pattern of TAPA–Tf film.

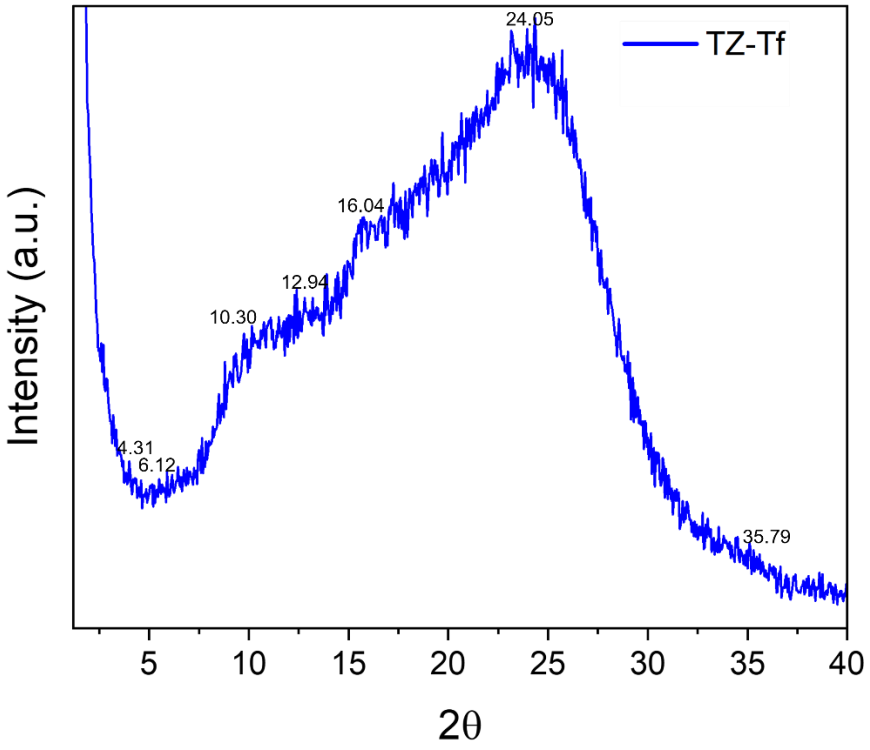


**Figure S19.** PXRD pattern of TZ–Tf film.

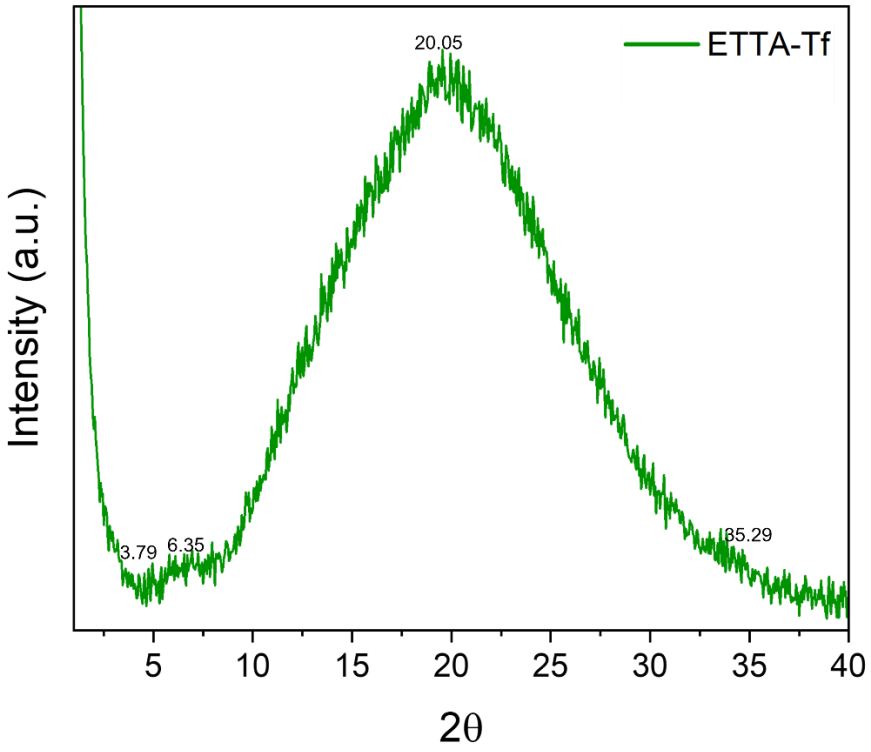


**Figure S20.** PXRD pattern of ETTA–Tf film.

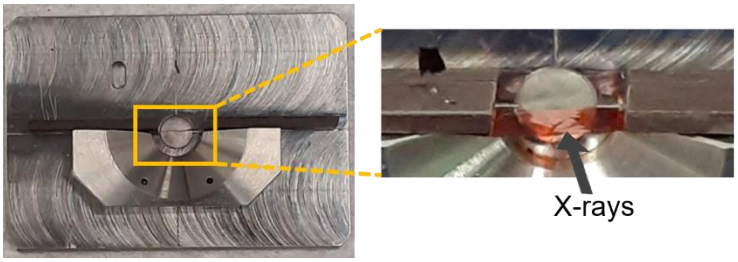


**Figure S21.** Image showing how 2D WAXS was performed on film cross-section. Bulk ETTA–Tf was cut into a very thin strip and placed onto the holder and pulled taunt on each side using magnets. 2D WAXs was then performed on film cross-section.

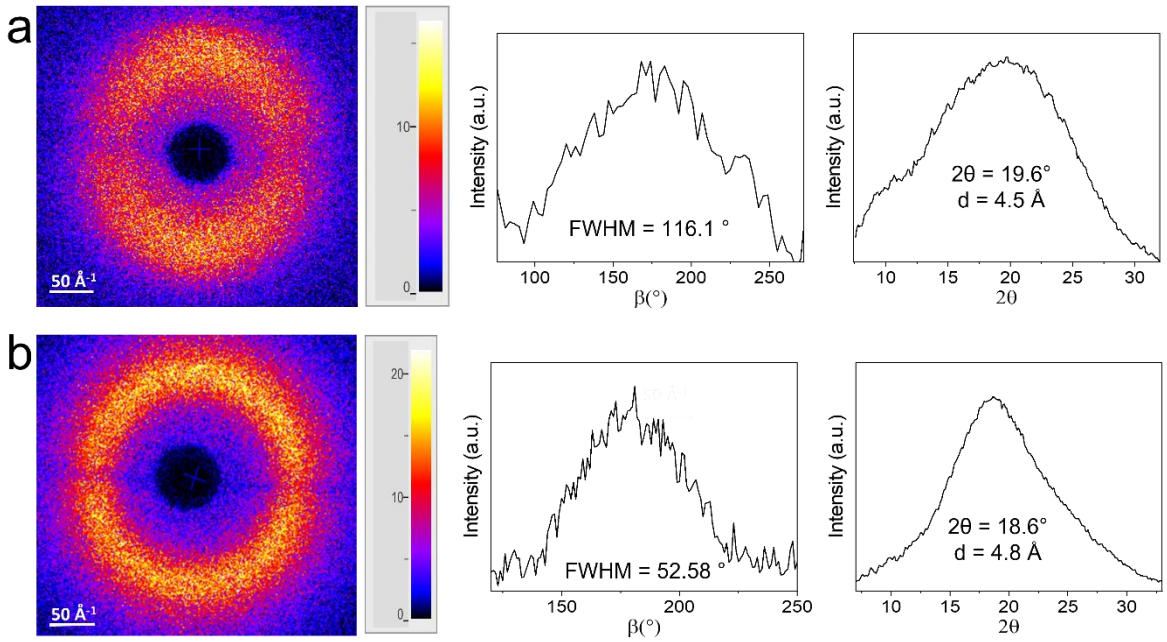


**Figure S22.** 2D WAXS was performed on a) fluorinated TAPB–Tf and b) non-fluorinated TAPB–TP films and radial average intensity and 2θ profiles were obtained from diffraction patterns. These diffraction patterns and profiles were then compared to better understand the effect of fluorine functionalization on microstructure and stacking of sheets along z-direction.

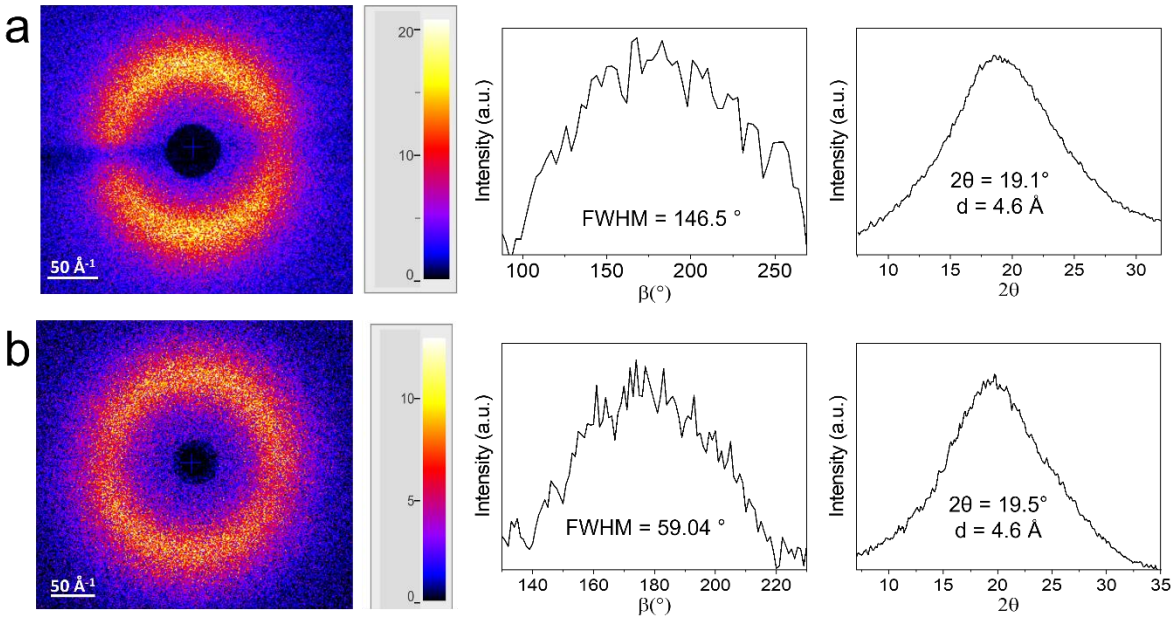


**Figure S23.** 2D WAXS was performed on a) fluorinated TAPA–Tf and b) non-fluorinated TAPA–TP films and radial average intensity and 2θ profiles were obtained from diffraction patterns. These diffraction patterns and profiles were then compared to better understand the effect of fluorine functionalization on microstructure and stacking of sheets along z-direction.

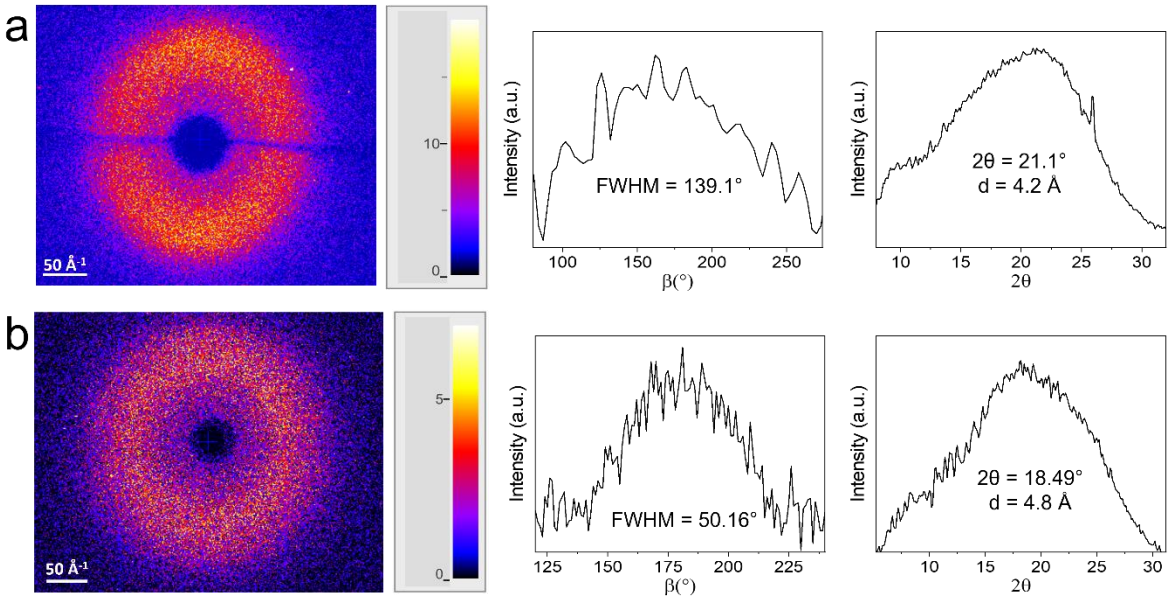


**Figure S24.** 2D WAXS was performed on a) fluorinated TZ–Tf and b) non-fluorinated TZ–TP films and radial average intensity and 2θ profiles were obtained from diffraction patterns. These diffraction patterns and profiles were then compared to better understand the effect of fluorine functionalization on microstructure and stacking of sheets along z-direction.

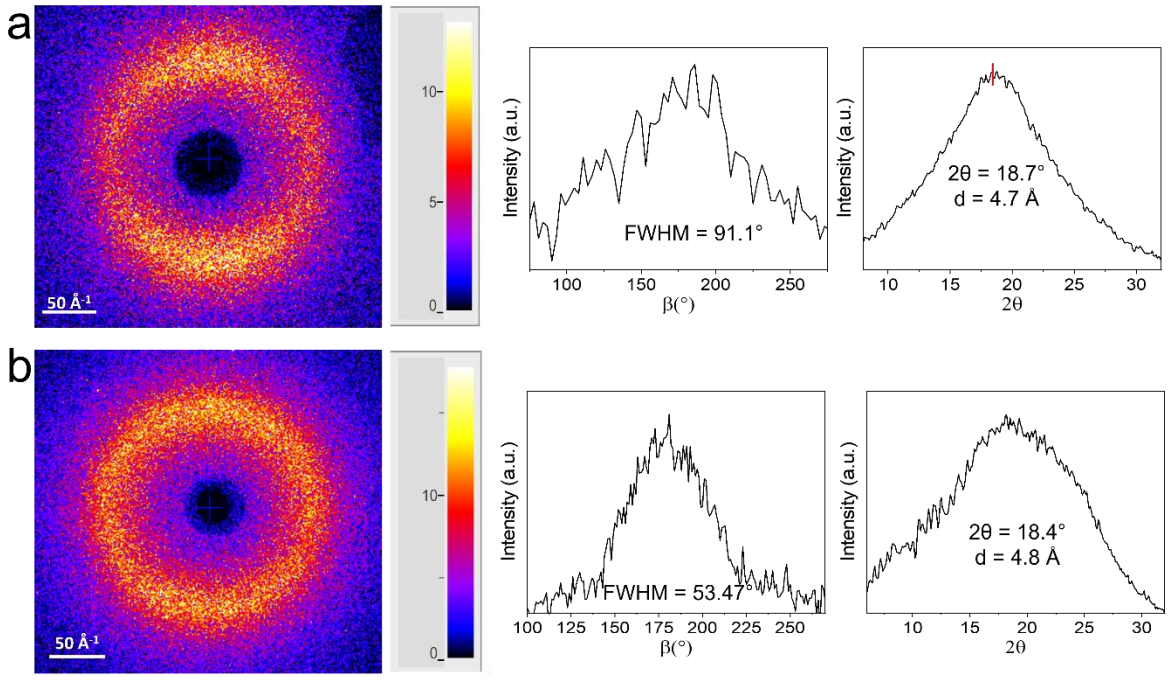


**Figure S25.** 2D WAXS was performed on a) fluorinated ETTA–Tf and b) non-fluorinated ETTA–TP films and radial average intensity and 2θ profiles were obtained from diffraction patterns. These diffraction patterns and profiles were then compared to better understand the effect of fluorine functionalization on microstructure and stacking of sheets along z-direction.

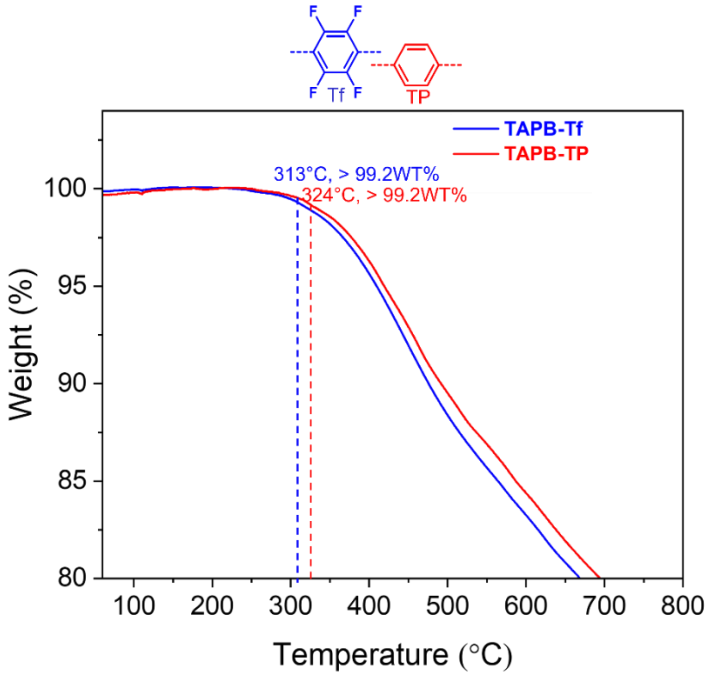


**Figure S26.** TGA was performed to compare thermostability between fluorinated TAPB–Tf and non-fluorinated TAPB–TP

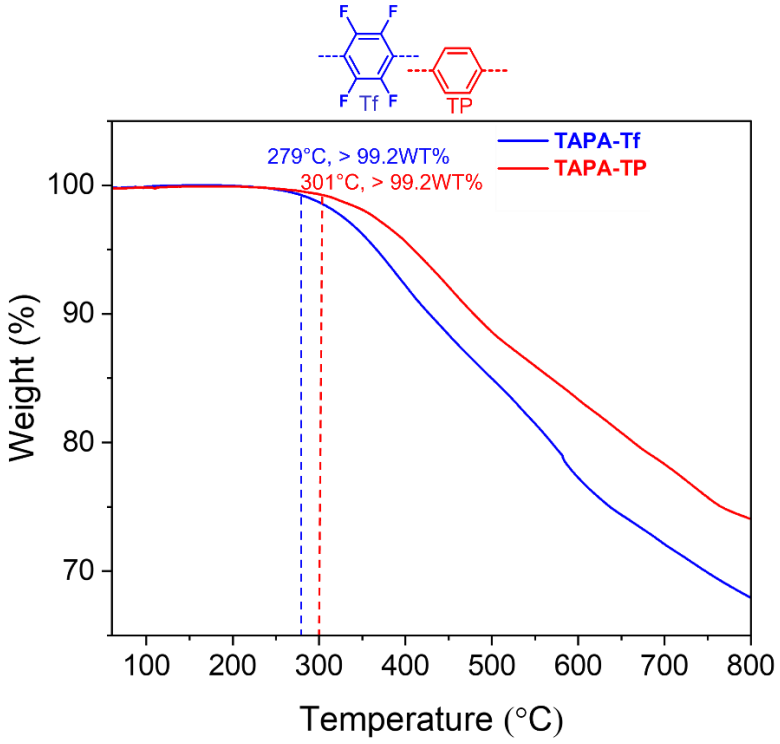


.

**Figure S27.** TGA was performed to compare thermostability between fluorinated TAPA–Tf and non-fluorinated TAPA–TP.

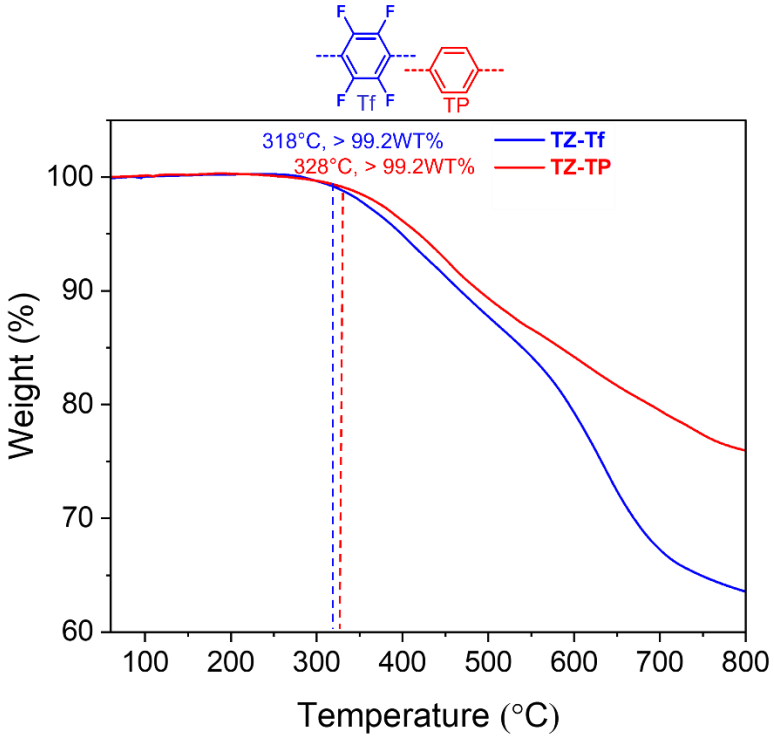


**Figure S28.** TGA was performed to compare thermostability between fluorinated TZ–Tf and non-fluorinated TZ–TP.

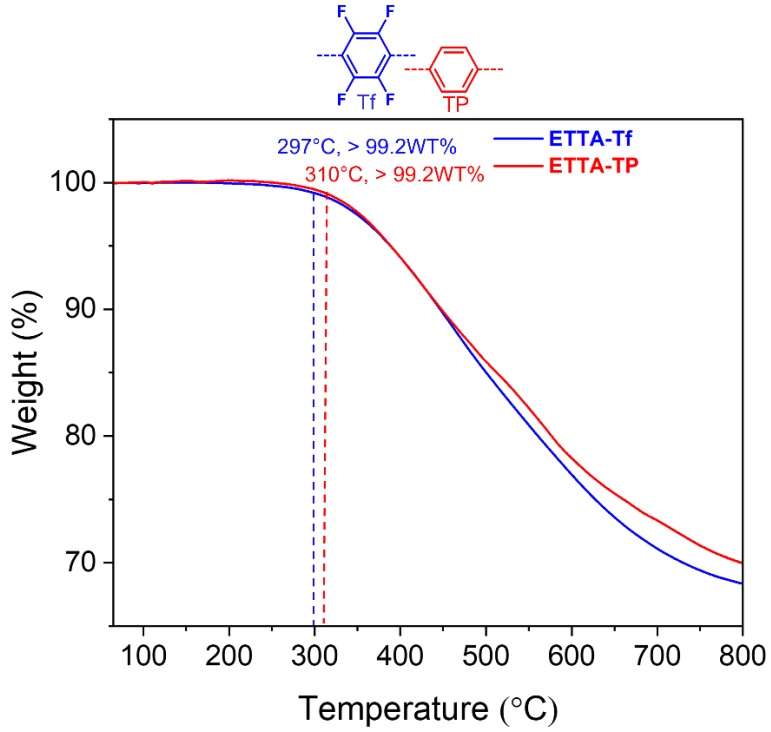


**Figure S29.** TGA was performed to compare thermostability between fluorinated ETTA–Tf and non-fluorinated ETTA–TP.

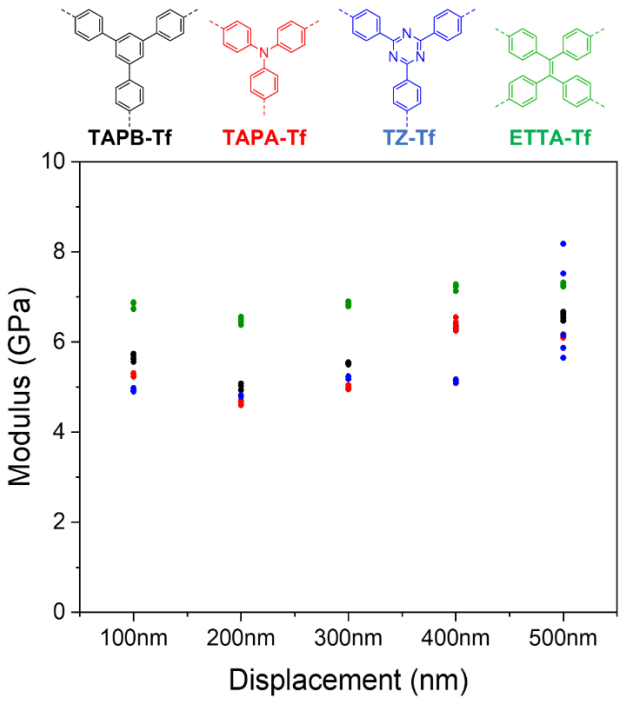


**Figure S30.** Nanoindentation was performed on all fluorinated films and compressive modulus was obtained using five indents at each depth displacement.

**Table S1.** Film average reduced compressive modulus (GPa) and calculated standard deviation at different each depth

| Depth (nm) | TAPB–Tf | TAPA–Tf | TZ–Tf | ETTA–Tf |
|---|---|---|---|---|
| **100** | 5.65 ± 0.071 | 5.27 ± 0.033 | 4.95 ± 0.036 | 6.82 ± 0.076 |
| **200** | 4.98 ± 0.067 | 4.65 ± 0.047 | 4.80 ± 0.013 | 6.47 ± 0.069 |
| **300** | 5.52 ± 0.019 | 5.00 ± 0.041 | 5.22 ± 0.025 | 6.84 ± 0.044 |
| **400** | 6.32 ± 0.019 | 6.39 ± 0.11 | 5.14 ± 0.038 | 7.23 ± 0.058 |
| **500** | 6.59 ± 0.082 | 6.12 ± 0.030 | 6.67 ± 1.11 | 7.27 ± 0.035 |

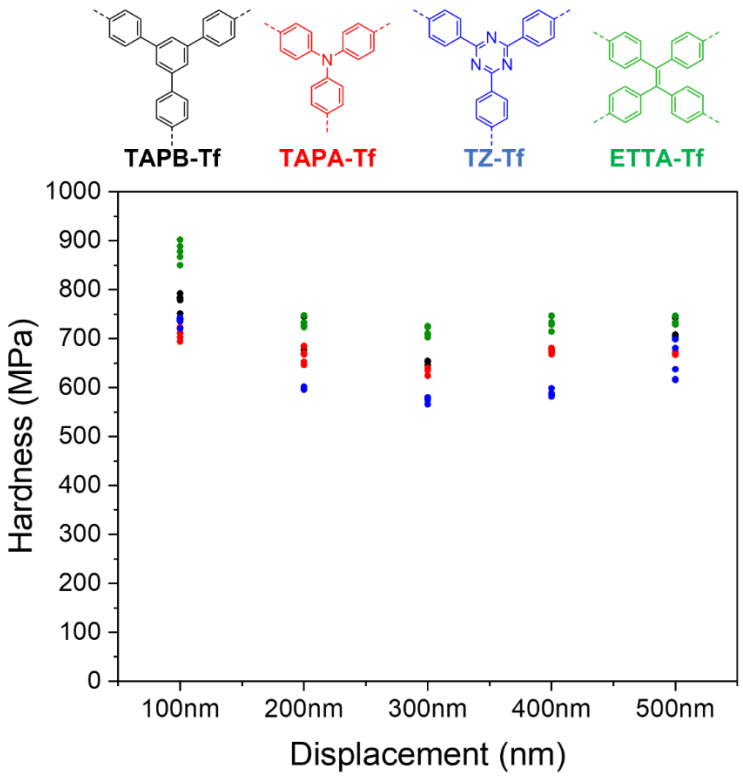


**Figure S31.** Nanoindentation was performed on all fluorinated films and compressive hardness was obtained using five indents at each depth displacement.

**Table S2.** Film average compressive Hardness (MPa) and calculated standard deviation at different depths

| Depth (nm) | TAPB–Tf | TAPA–Tf | TZ–Tf | ETTA–Tf |
|---|---|---|---|---|
| **100** | 777.83 ± 15.57 | 714.42 ± 17.76 | 735.68 ± 8.92 | 877.49 ± 19.97 |
| **200** | 701.55 ± 34.36 | 664.68 ± 15.44 | 598.47 ± 2.33 | 731.11 ± 9.87 |
| **300** | 648.66 ± 8.08 | 632.66 ± 7.70 | 575.45 ± 5.57 | 714.49 ± 9.92 |
| **400** | 674.68 ± 3.63 | 675.20 ± 5.34 | 587.92 ± 6.56 | 733.95 ± 13.58 |
| **500** | 712.00 ± 17.63 | 669.11 ± 2.53 | 650.09 ± 37.88 | 737.75 ± 8.36 |

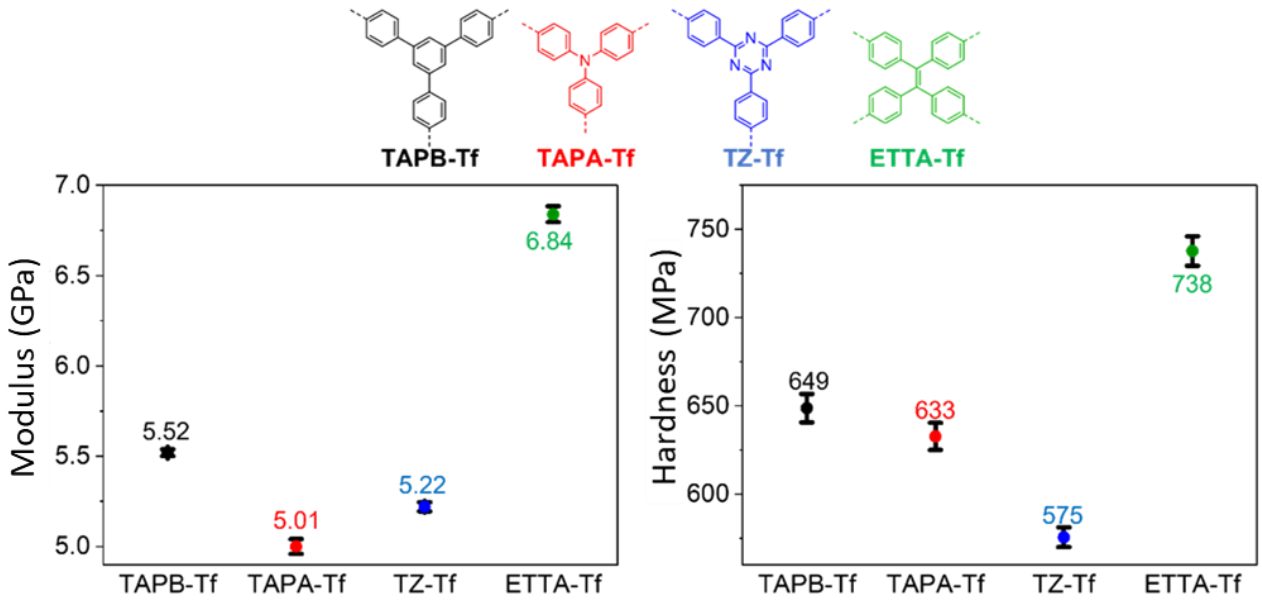


**Figure S32.** Nanoindentation average compressive modulus and average compressive hardness for all fluorinated films taken at 10% depth displacement of total film thickness.

**Table S3.** Comparison of nanomechanical properties of materials used for separation performance applications

| Material (thin films) | Compressive Modulus (GPa) | Compressive Hardness (MPa) | Reference |
|---|---|---|---|
| Nafion 117 | 0.12- 0.23 | 13 - 30 | [2] |
| Nylon | 1.2-2.5 | 60-120 | [3] |
| Poly(vinyl alcohol) | 2.5-3.0 | 150-200 | [4] |
| Polyvinylidene fluoride | 0.48-1.8 | 23-93 | [5] |
| Polyarmid | 2.8-5.3 | 70-290 | [3] |
| Polyethersulfone | 2.6-3.5 | 200-250 | [6] |
| Polyimide | 5-12 | 300-800 | [3,7] |
| HKUST-1MOF | 11.4-18 | 200-230 | [3] |
| Cu(CHDA)MOF | 10.9 | 460 | [3] |
| ZIF-NaX FAU | 2.75-12.5 | 800 | [8] |
| ZIF-8 | 3.2 | 531 | [9,10] |

| | | | |
|---|---|---|---|
| Graphene | 37 | 10,000 | [11] |
| Fluorinated-2D-C-POPs | 3.4-3.3 | 210-330 | [12] |
| Benzoxaole-2D-C-POPs | 6.4-8.0 | 580-660 | [3] |
| **Imine-2D-C-POPs** | 5.54-7.49 | 438-630 | [1] |
| **F-Imine-2D-C-POPs** | 5.01-6.84 | 575-738 | This Work |

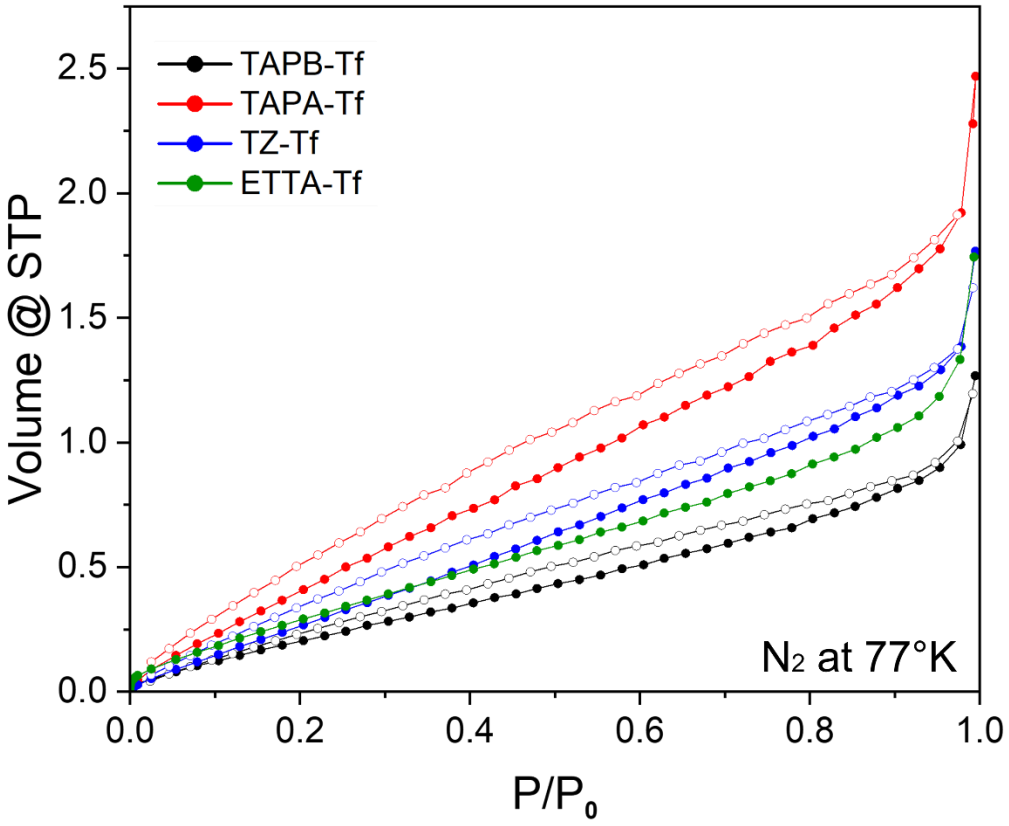


**Figure S33.** BET $N_2$ adsorption-desorption isotherms of fluorinated films taken at 77 K.

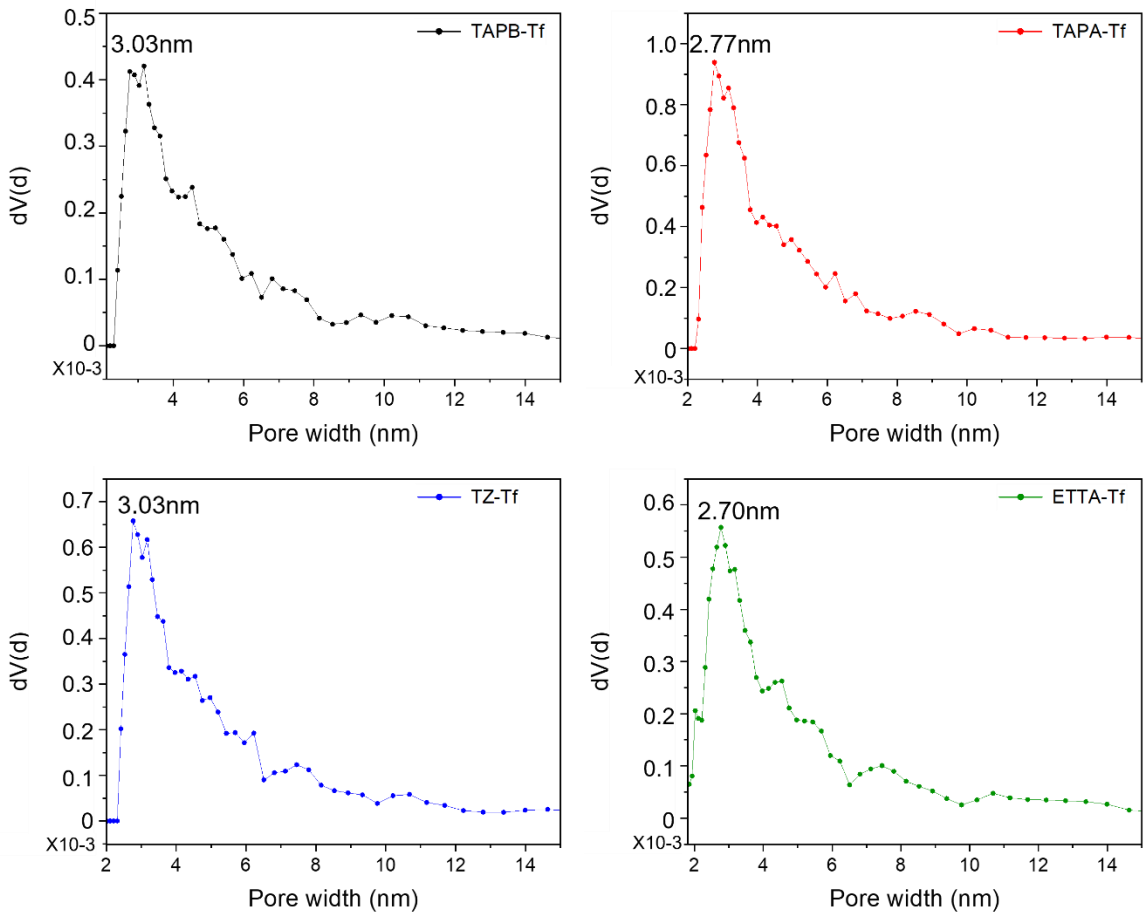


**Figure S34.** Fluorinated films pore width distribution obtained from $N_2$ adsorption measurements at 77 K using NLDFT model.

For films of larger surface areas, the solvent to molar ratios were maintained with adjustments made with the volume of drop-casted precursor solution. Film thickness could be tuned by adjusting the ratio of starting monomer to solvent. It was observed that the thickness could decreased by 3-5x's by changing the starting concentration to 0.25x concentration (**Figure S5-S8**).

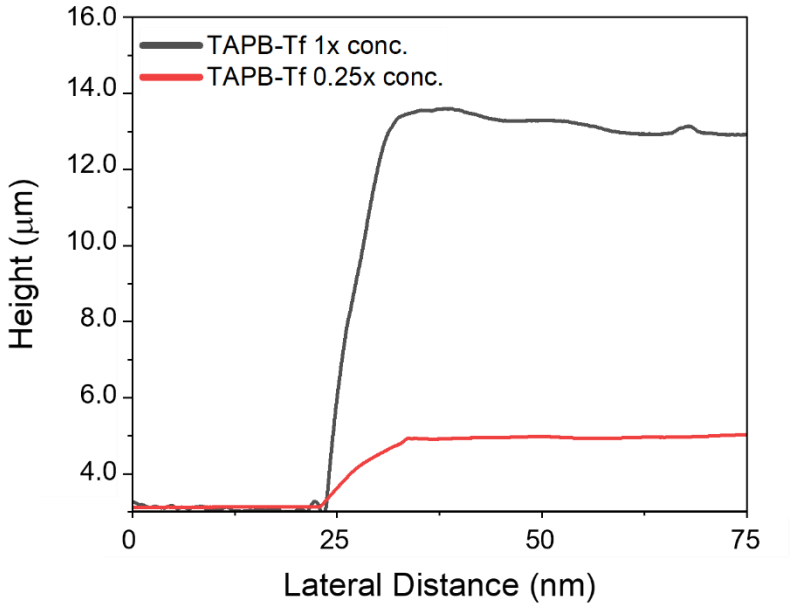


**Figure S35.** Profilometer was used to obtain height profiles for TAPB–Tf films formed using 1x and 0.25x starting monomer concentration.

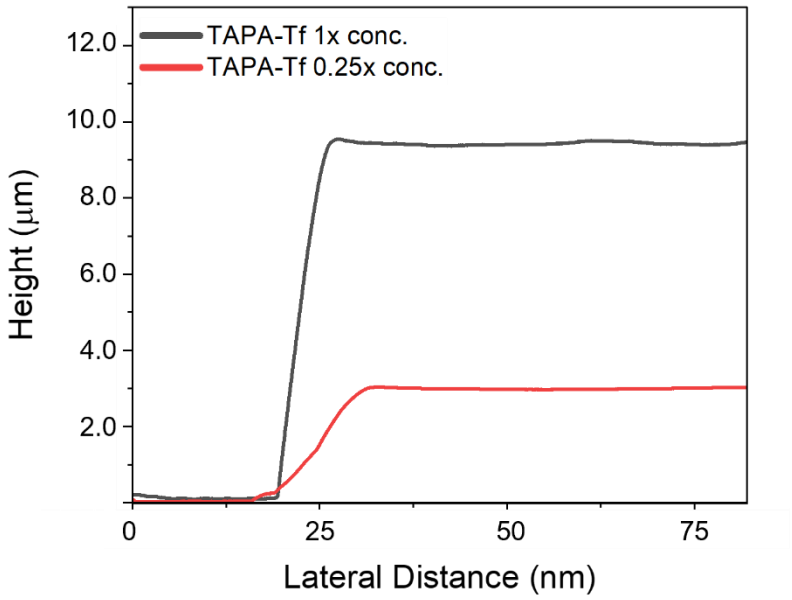


**Figure S36.** Profilometer was used to obtain height profiles for TAPA–Tf films formed using 1x and 0.25x starting monomer concentration.

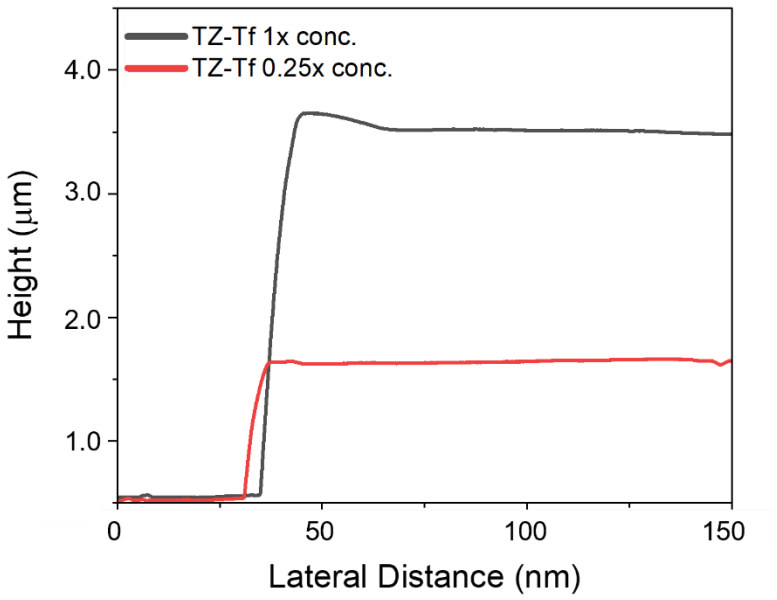


**Figure S37.** Profilometer was used to obtain height profiles for TZ–Tf films formed using 1x and 0.25x starting monomer concentration.

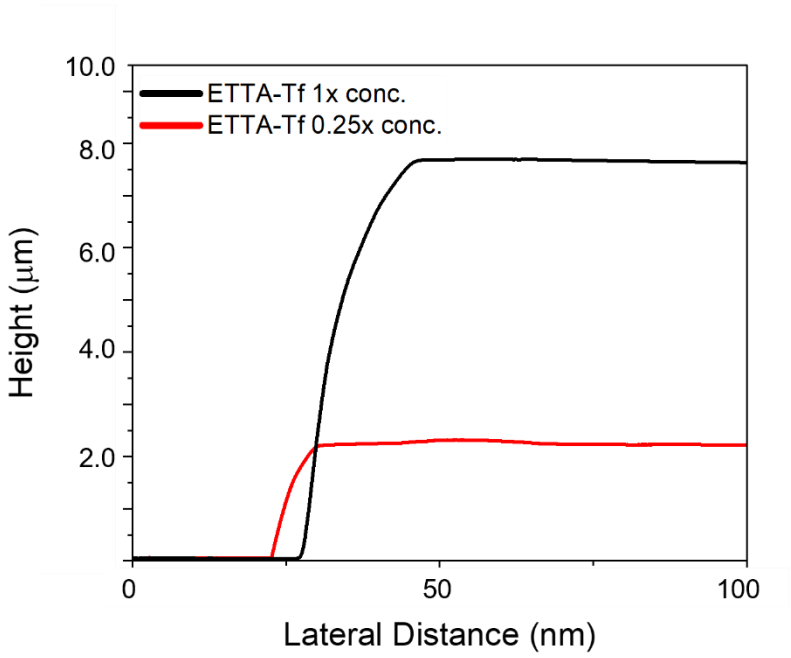


**Figure S38.** Profilometer was used to obtain height profiles for ETTA–Tf films formed using 1x and 0.25x starting monomer concentration.

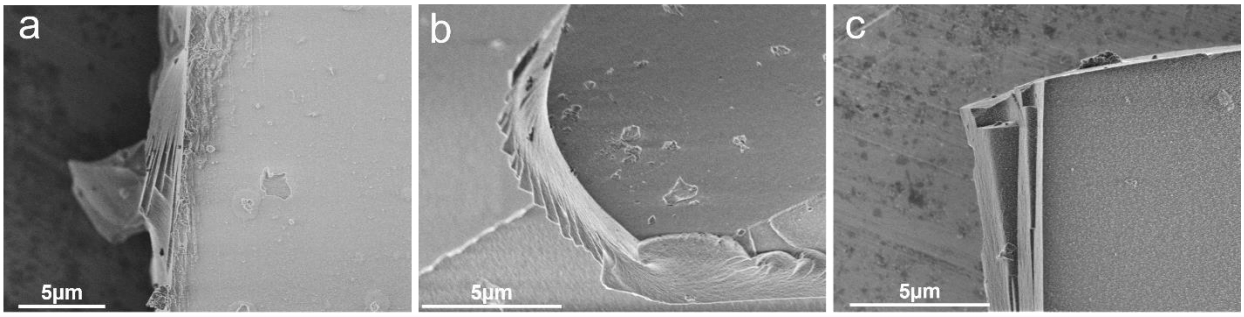


**Figure S39.** SEM of a) TAPB–Tf, b) TZ–Tf, and c) ETTA–Tf bulk film showing film surface morphology. The fractured film edge shows films to be composed of layered structures.

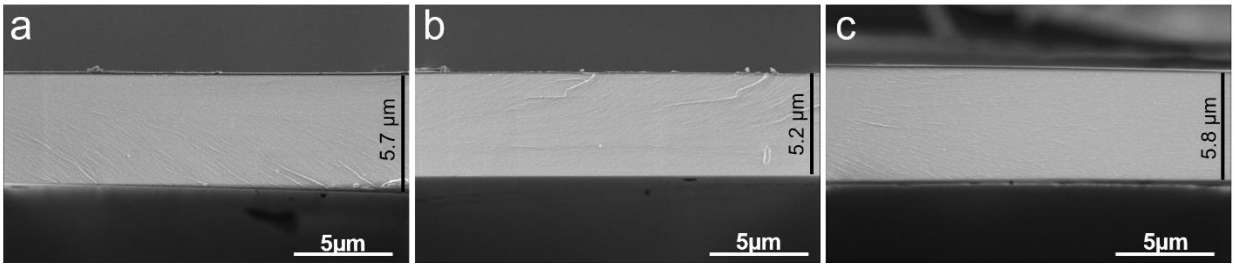


**Figure S40.** SEM of a) TAPA–Tf, b) TZ–Tf, and c) ETTA–Tf bulk film cross-section showing uniformed and smooth surface.

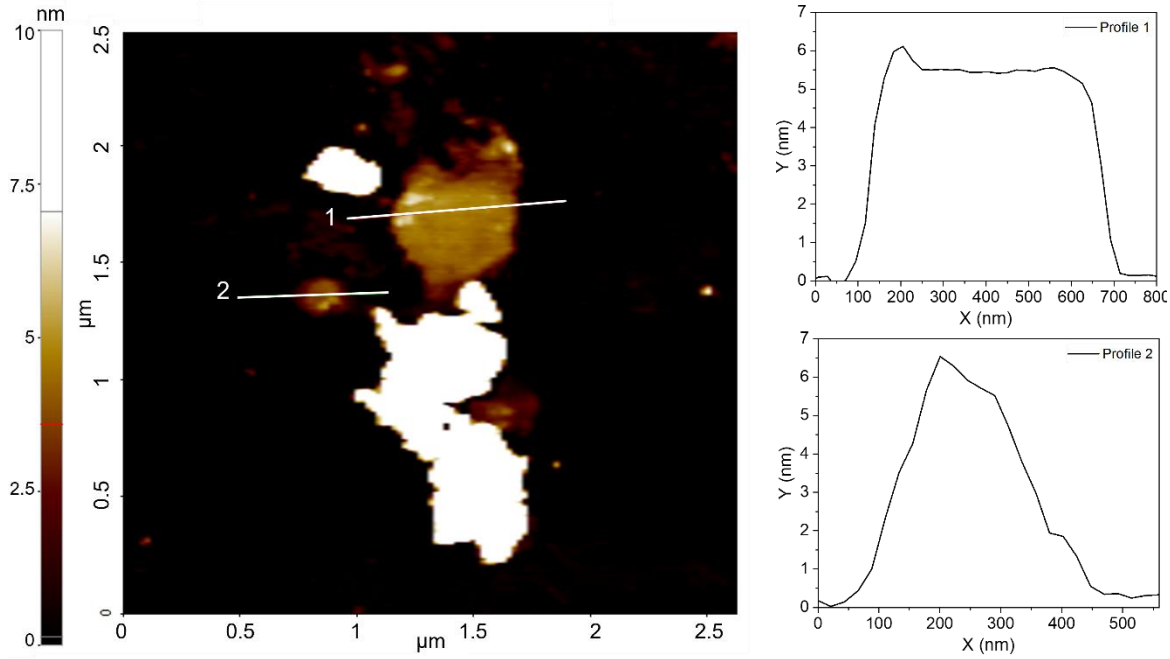


**Figure S41.** AFM micrograph and corresponding height profile for exfoliated TAPB–Tf film.

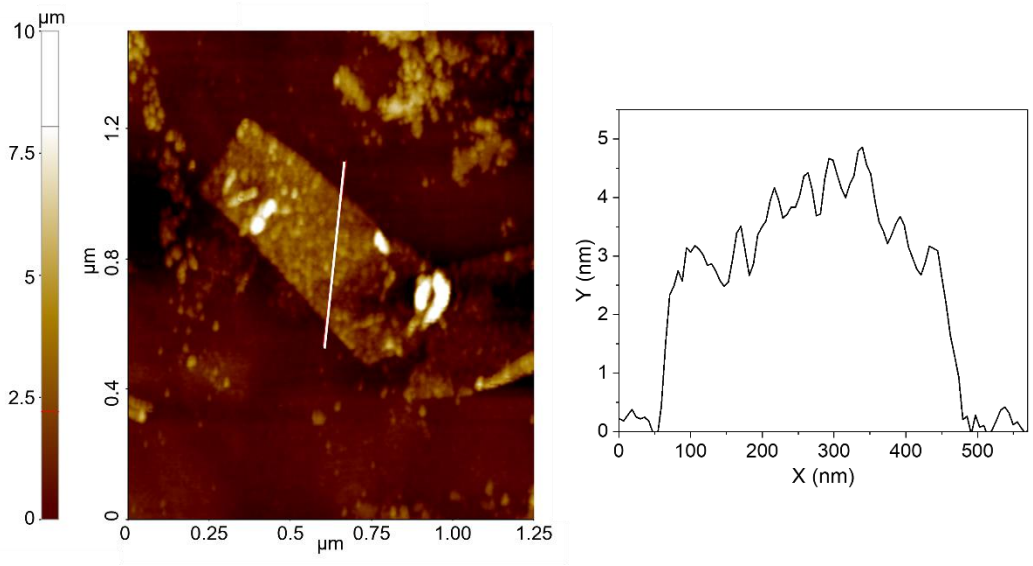


**Figure S42.** AFM micrograph and corresponding height profile for exfoliated TAPA–Tf film.

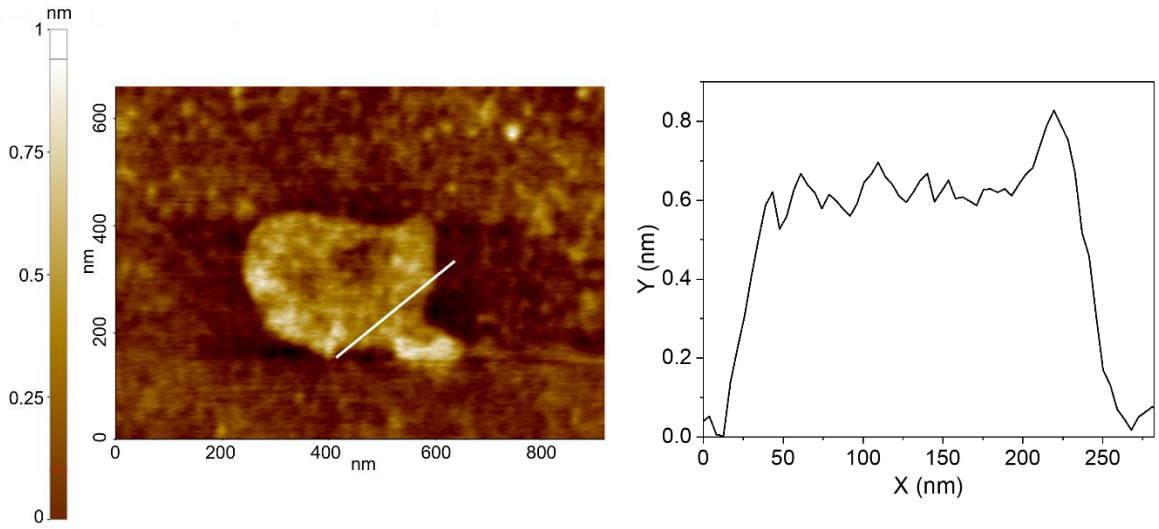


**Figure S43.** AFM micrograph and corresponding height profile for exfoliated TZ–Tf film.

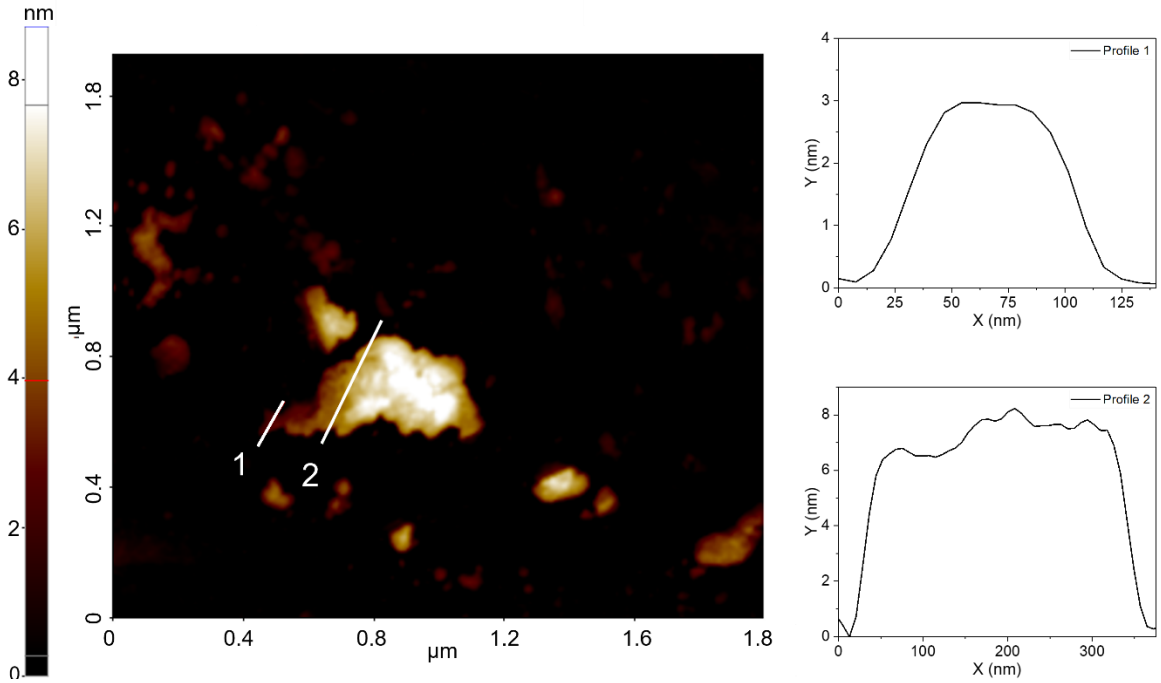


**Figure S44.** AFM micrograph and corresponding height profile for exfoliated TZ–Tf film.

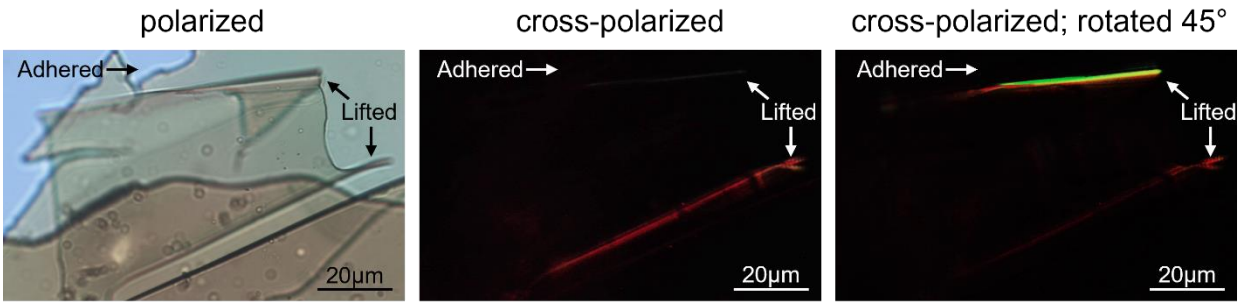


**Figure S45.** Polarizing optical microscopy was performed on TAPB–Tf film pieces. Birefringence was observed with cross-polarized light on the portion of the film that was lifted, a result of out-of-plane anisotropy. Adhered films showed no birefringence due to in-plane isotropy.

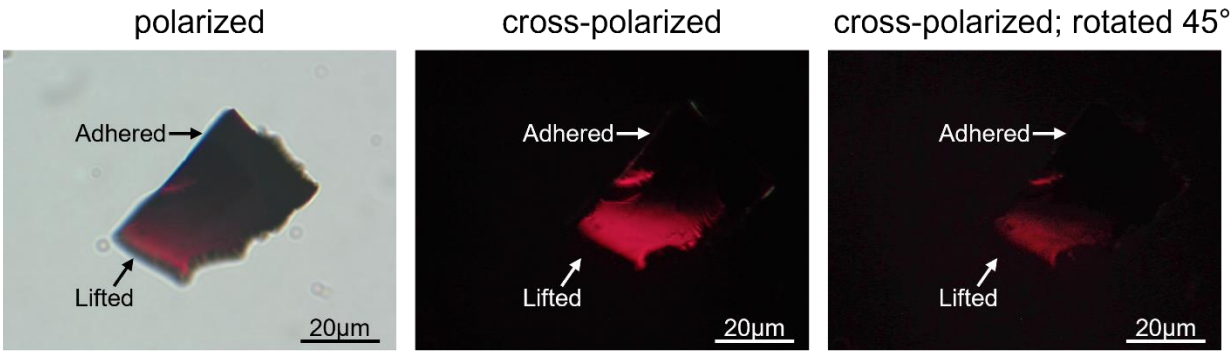


**Figure S46.** Polarizing optical microscopy was performed on TAPA–Tf film pieces. Birefringence was observed with cross-polarized light on the portion of the film that was lifted, a result of out-of-plane anisotropy. Adhered films showed no birefringence due to in-plane isotropy.

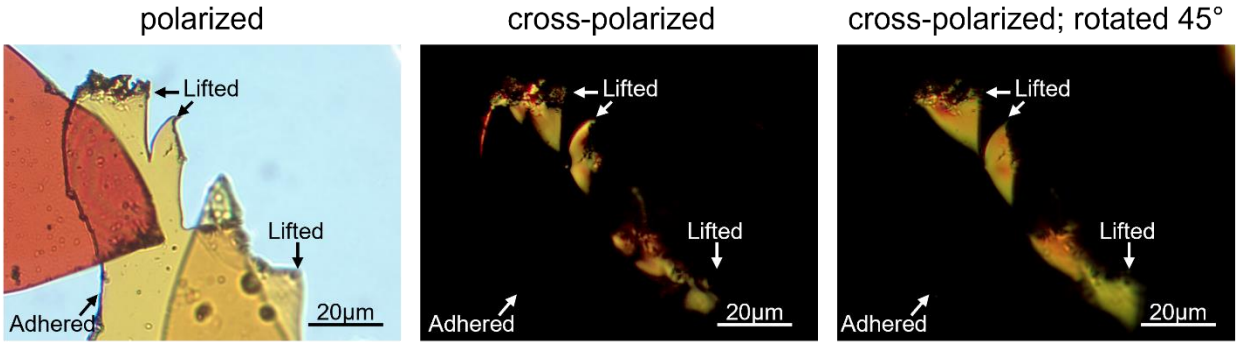


**Figure S47.** Polarizing optical microscopy was performed on ETTA–Tf film pieces. Birefringence was observed with cross-polarized light on the portion of the film that was lifted, a result of out-of-plane anisotropy. Adhered films showed no birefringence due to in-plane isotropy.

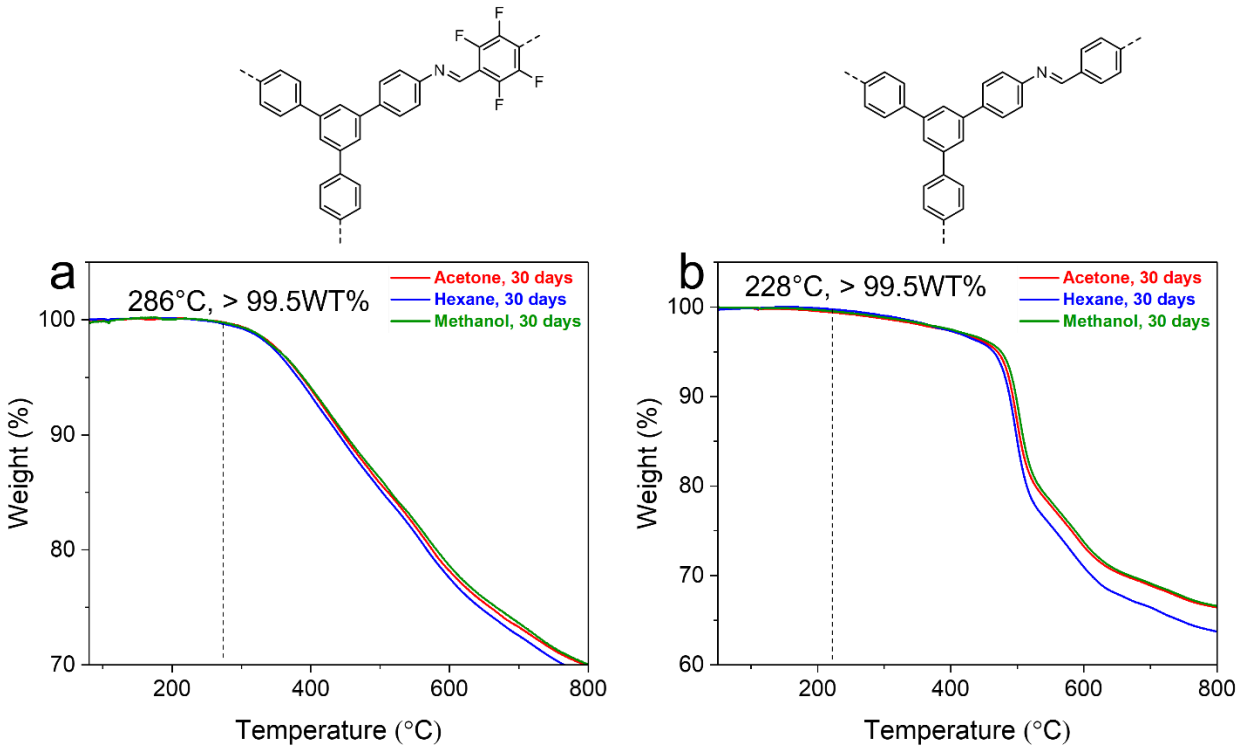


**Figure S48.** TGA of a) TAPP–Tf and b) TAPP–TP film showing thermal stability after immersed in acetone, hexane, or methanol for 30 days.

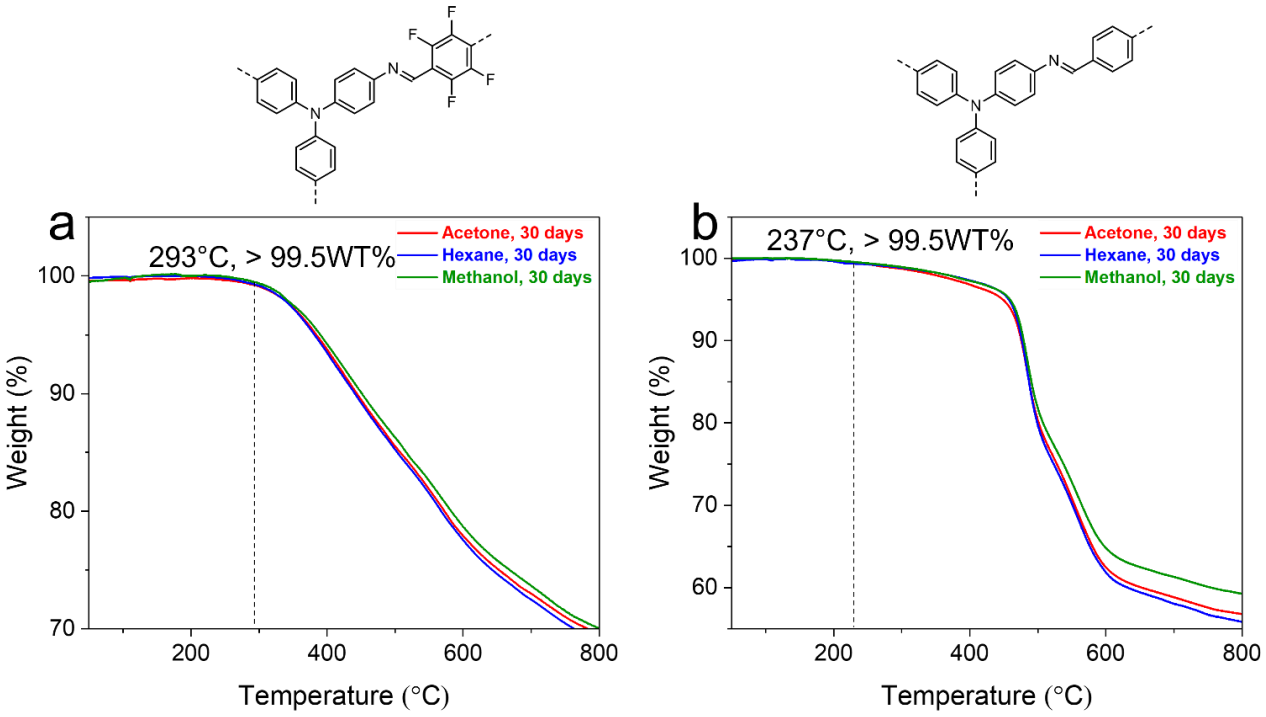


**Figure S49.** TGA of a) TAPA–Tf and b) TAPA–TP film showing thermal stability after immersed in acetone, hexane, or methanol for 30 days.

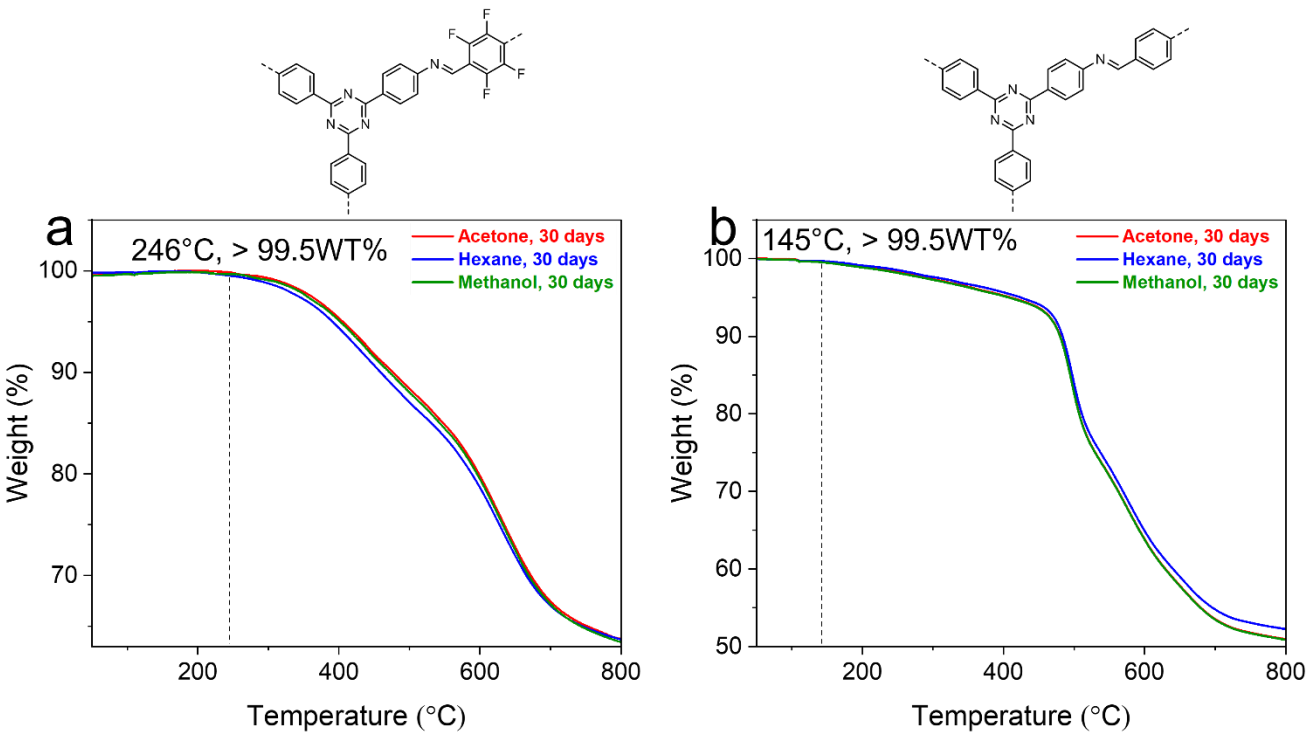


**Figure S50.** TGA of a) TZ–Tf and b) TZ–TP film showing thermal stability after immersed in acetone, hexane, or methanol for 30 days.

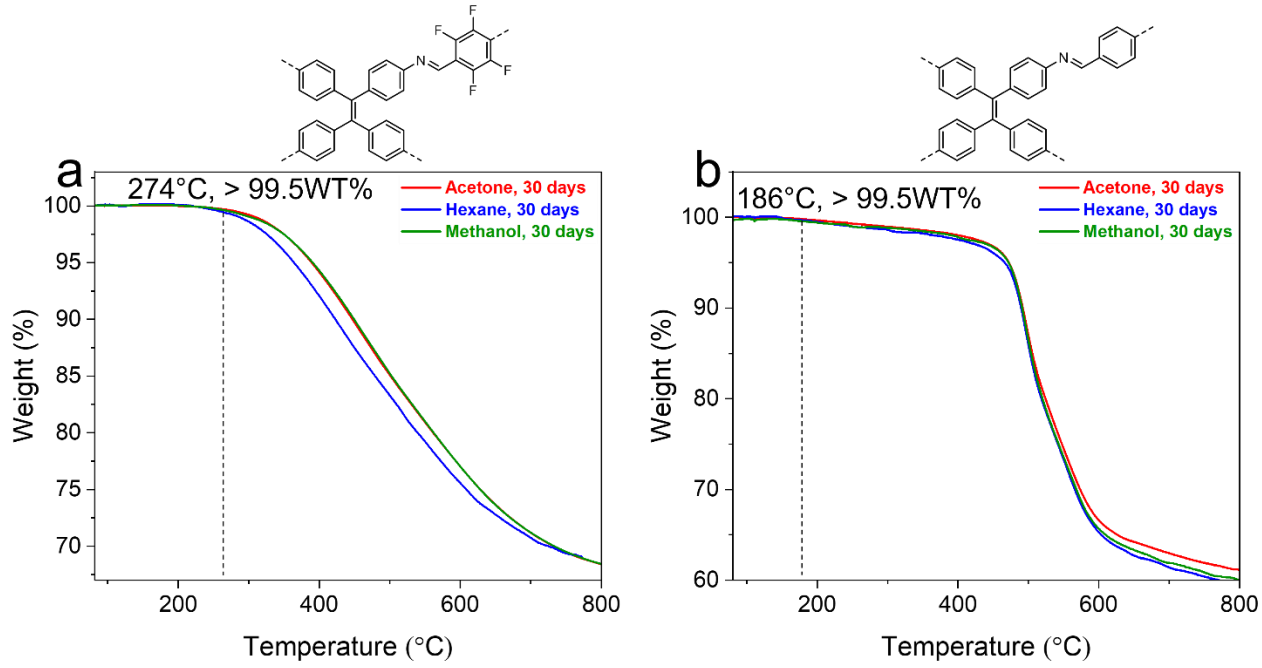


**Figure S51.** TGA of a) ETTA–Tf and b) ETTA–TP film showing thermal stability after immersed in acetone, hexane, or methanol for 30 days.

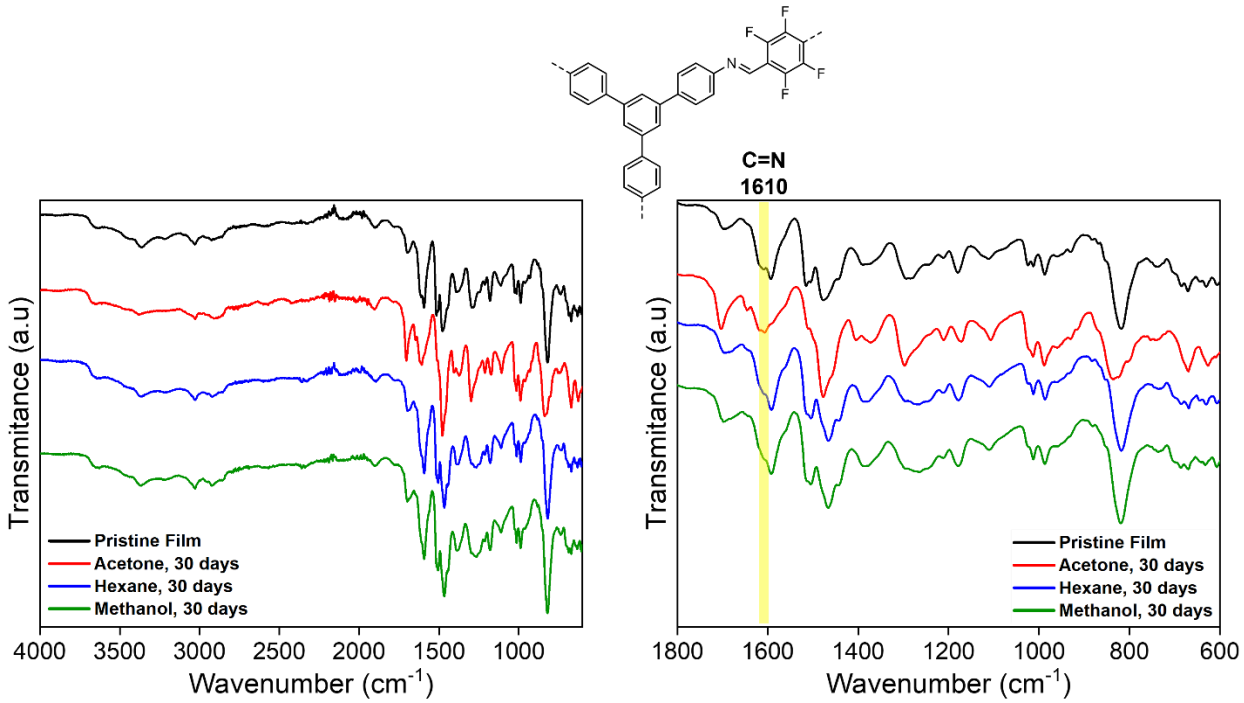


**Figure S52.** FTIR of TAPB–Tf showing imine bond stability after immersed in acetone, hexane, or methanol for 30 days.

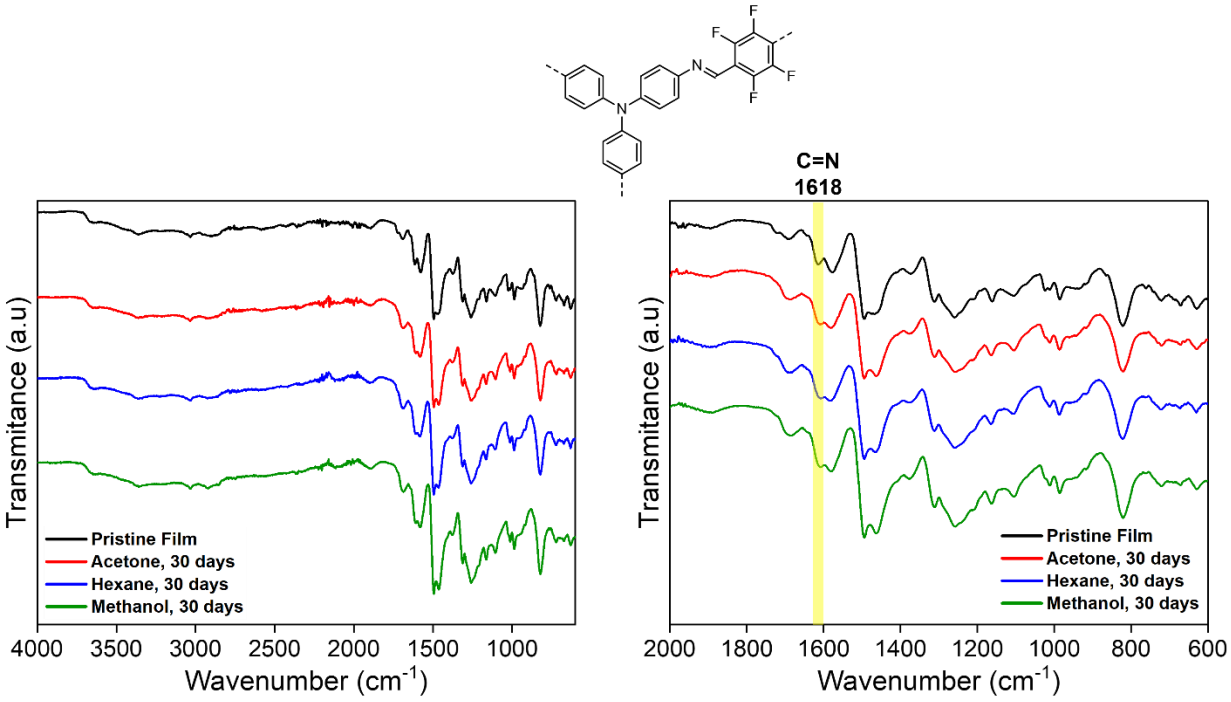


**Figure S53.** FTIR of TAPA–Tf showing imine bond stability after immersed in acetone, hexane, or methanol for 30 days.

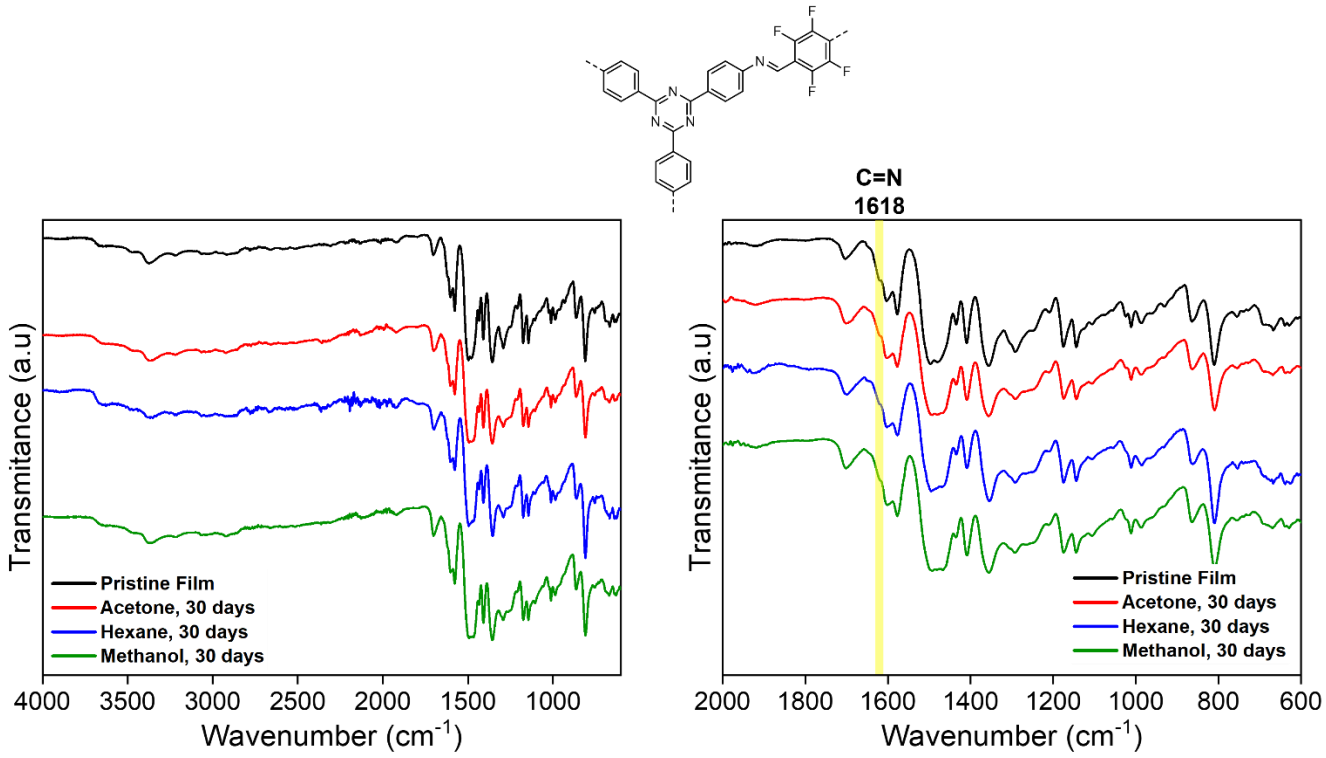


**Figure S54.** FTIR of TZ–Tf showing imine bond stability after immersed in acetone, hexane, or methanol for 30 days.

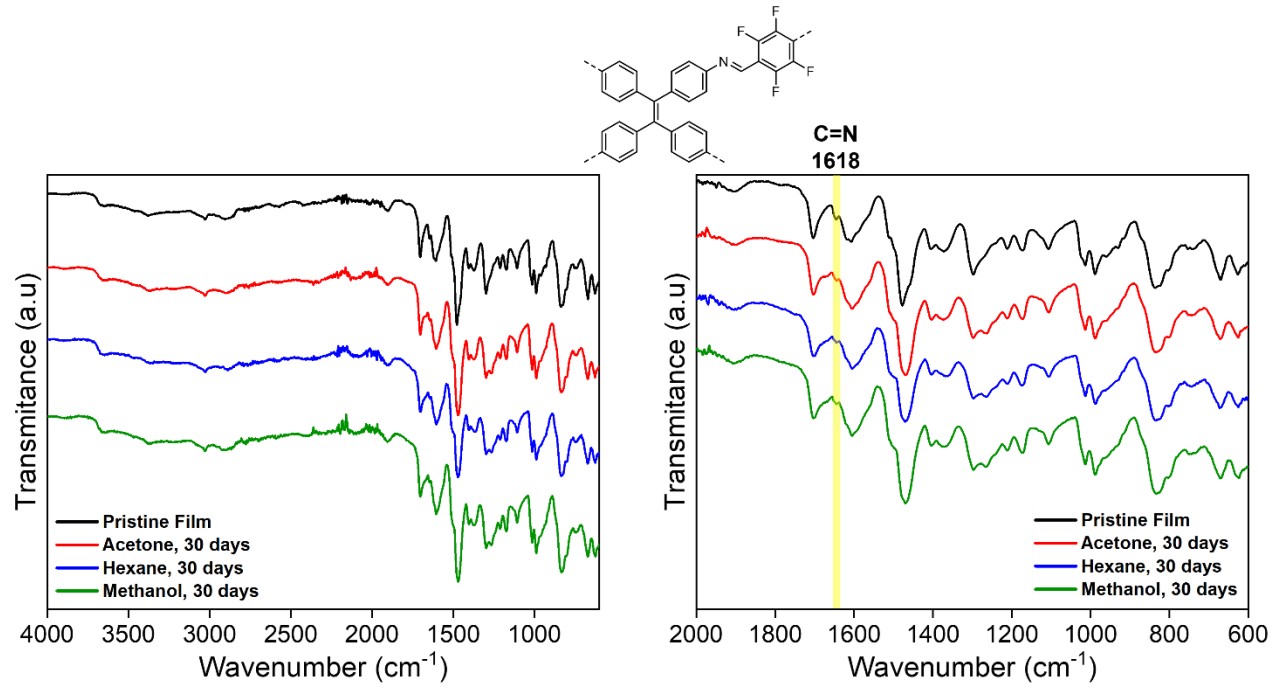


**Figure S55.** FTIR of ETTA–Tf showing imine bond stability after immersed in acetone, hexane, or methanol for 30 days.

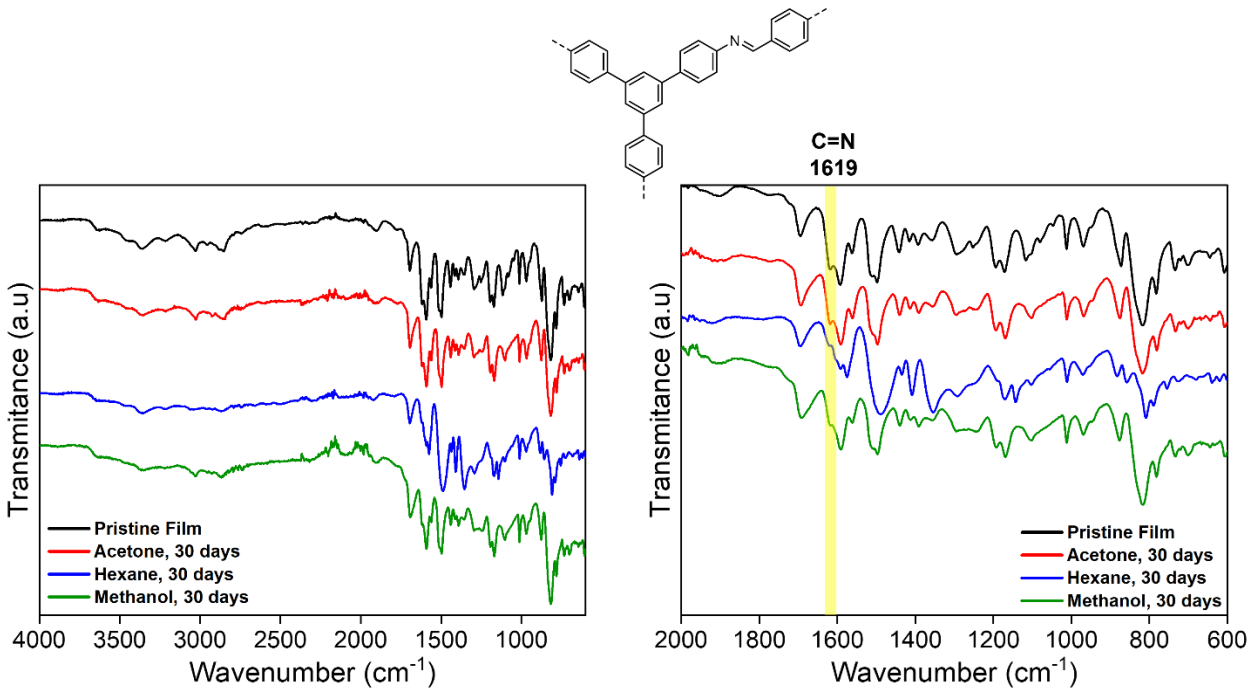


**Figure S56.** FTIR of TAPB–TP showing imine bond stability after immersed in acetone, hexane, or methanol for 30 days.

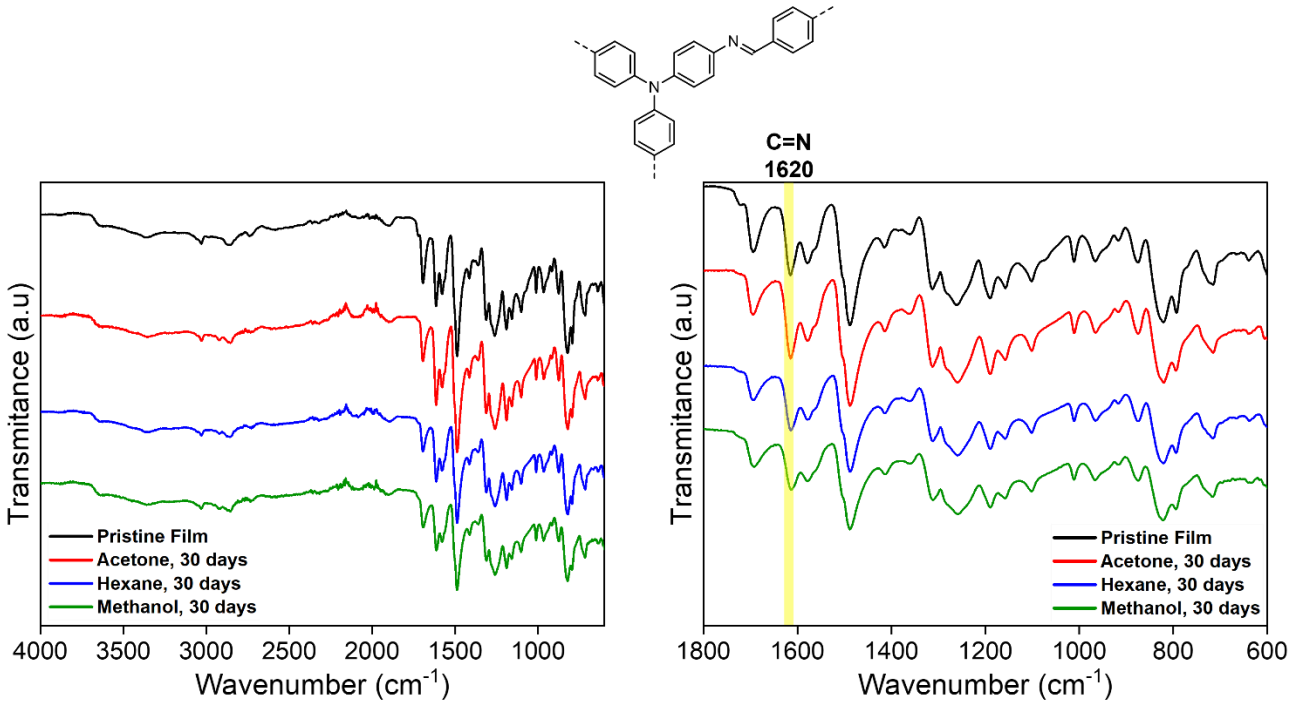


**Figure S57.** FTIR of TAPA–TP showing imine bond stability after immersed in acetone, hexane, or methanol for 30 days.

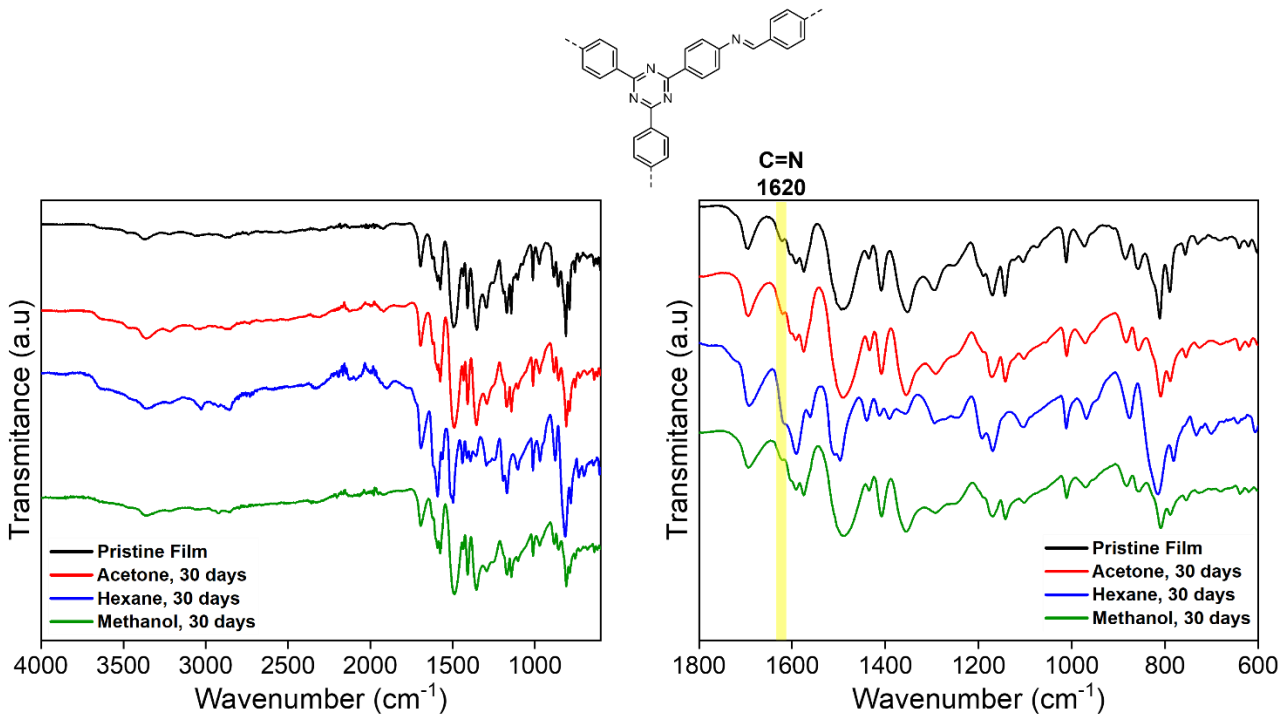


**Figure S58.** FTIR of TZ–TP showing imine bond stability after immersed in acetone, hexane, or methanol for 30 days.

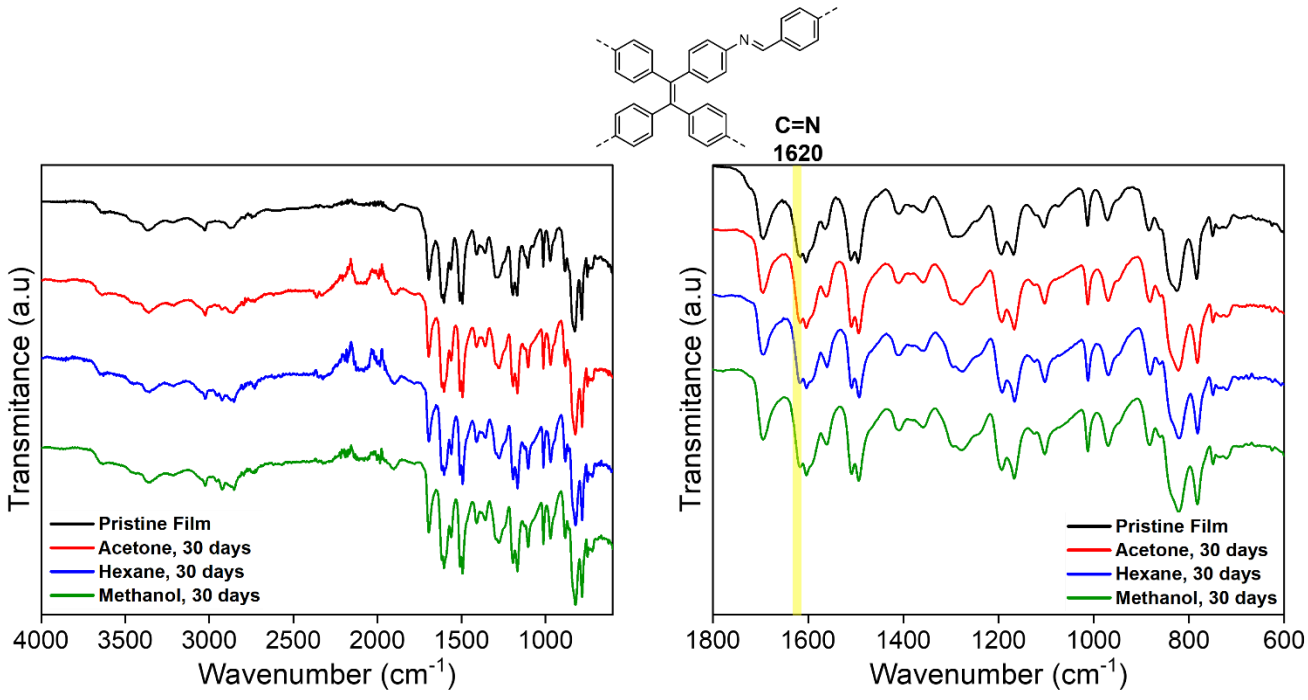


**Figure S59.** FTIR of ETTA–TP showing imine bond stability after immersed in acetone, hexane, or methanol for 30 days.

# 3. Predicted and experimental nanofiltration studies

## *3.1. Theoretical model of nanofiltration*

The pore flow model developed by Bowen and Welfoot was used to describe the nanofiltration process.[13] The most important assumptions and equations are discussed below. For a more detailed description of the model and a comparison between the model and other nanofiltration models, the reader is referred to Bowen and Welfoot,[13] Silva and Livingston,[14] and Santos *et al*.[15] The model presumes that the membrane has a selective layer with a uniform $\Delta x$ thickness and that the selective layer is solely responsible for both the selectivity and flow resistance of the membrane. Laminar solution flux occurs through unconnected cylindrical pores perpendicular to the plane of the membrane. The average fluid velocity ($V$) can be described by the Hagen–Poiseuille equation:

$$V = \frac{r_\mathrm{p}^2 \, \Delta P_e}{8\eta \, \Delta x} \qquad \text{Eq. 1,}$$

where $r_\mathrm{p}$ is the pore radius, $\Delta P_e$ is the effective pressure difference between the two sides of the membrane, and η is the solution viscosity equal to the solvent viscosity at low concentrations. $\Delta P_\mathrm{e}$ is the difference between the applied transmembrane pressure ($\Delta P$) and the osmotic pressure difference ($\Delta\pi$). In dilute organic solutions with uncharged solutes, the osmotic pressure is negligible compared to the applied transmembrane pressure, and thus $\Delta P_\mathrm{e}$ equals $\Delta P$. The uncharged solute flux ($j_\mathrm{s}$) at a certain point inside the membrane is the sum of convectional and diffusional terms. The convectional term is directly proportional to the product of the fluid velocity and solute concentration ($c = c(x)$) at that point. The coefficient of proportionality is the uncharged solute-hindrance factor for convection ($K_\mathrm{c}$). The diffusional term can be described by Fick's one-dimensional first law, assuming that there is an ideal solution and there is no radial diffusion:

$$j_\mathrm{s} = K_\mathrm{c} c V - \frac{D_\mathrm{p} c}{RT} \frac{\mathrm{d}\mu}{\mathrm{d}x} \qquad \text{Eq. 2,}$$

where $D_\mathrm{p}$ is the pore diffusion coefficient, $R$ is the universal gas constant (8.314 J $\mathrm{K^{-1}}$ $\mathrm{mol^{-1}}$), $T$ is the absolute temperature, $\mu$ is the chemical potential, and $x$ is the cross-membrane coordinates.

Under ideal solutions and isothermal conditions, the chemical potential is consisting of concentration-dependent, pressure-dependent, and constant terms.

$$\mu = RT \ln c + V_\mathrm{s}\, P + constant \qquad \text{Eq. 3,}$$

where $V_\mathrm{s}$ is the molar volume of the solute, and $P$ is the pressure. At equilibrium, the solute flux can also be written as the product of the permeate concentration ($C_\mathrm{p}$) and fluid velocity. Therefore, by combining Eqs. 1–3, assuming a constant pressure gradient, results in the following differential equation:

$$\frac{\mathrm{d}c}{\mathrm{d}x} = \frac{V}{D_\mathrm{p}}\left[\left(K_\mathrm{c} - \frac{D_\mathrm{p} V_\mathrm{s} 8\eta}{RT r_\mathrm{p}^2}\right)c - C_\mathrm{p}\right] = \frac{V}{D_\mathrm{p}}\left[(K_\mathrm{c} - Y)c - C_\mathrm{p}\right]. \qquad \text{Eq. 4}$$

For simplicity, $Y$ is often introduced to denote the coefficient of the pressure-induced diffusion term. The differential equation can be integrated for the length of the membrane pores, i.e., between 0 and the membrane thickness ($\Delta x$). The pore concentration boundaries are accordingly the feed and permeate concentrations multiplied by the steric partitioning coefficient ($\varphi$).

$$\int_{\phi C_f}^{\phi C_p} \frac{1}{(K_c - Y)c - C_p}\,\mathrm{d}c = \int_0^{\Delta x} \frac{V}{D_p}\,\mathrm{d}x \qquad \text{Eq. 5}$$

Integration and rearrangement results in an equation that correlates the permeate and feed concentrations.

$$\frac{C_\mathrm{p}}{C_\mathrm{f}} = \frac{(K_\mathrm{c} - Y)\phi \cdot \mathrm{e}^{\frac{(K_\mathrm{c}-Y)V\Delta x}{D_\mathrm{p}}}}{(K_\mathrm{c} - Y)\phi - 1 + \mathrm{e}^{\frac{(K_\mathrm{c}-Y)V\Delta x}{D_\mathrm{p}}}} = \frac{(K_\mathrm{c} - Y)\phi \cdot \mathrm{e}^{Pe'}}{(K_\mathrm{c} - Y)\phi - 1 + \mathrm{e}^{Pe'}} \qquad \text{Eq. 6}$$

The exponent is often defined as the modified Peclet number (*Pe'*). *Pe'* can be written in a different form by expressing $V\Delta x$ using the Hagen–Poiseuille equation. After rearranging the equation and inserting the definition of rejection, one can arrive at the following equation, which allows the calculation of rejections according to the pore flow model.

$$R = 1 - \frac{(K_\mathrm{c} - Y)\phi}{1 - [1 - (K_\mathrm{c} - Y)\phi] \cdot \mathrm{e}^{-Pe'}} \qquad \text{Eq. 7}$$

*Y* and *Pe'* both contain the product of pore viscosity and the pore diffusion coefficient. This product is directly proportional to the bulk parameters through the hindrance factor for diffusion ($K_d$).

$$D_p\eta = K_d D_\infty \eta_0 \qquad \text{Eq. 8}$$

Therefore, *Y* and *Pe'* can be written as follows.

$$Y = \frac{8K_d D_\infty \eta_0}{RTr_p^2} V_s \qquad \text{Eq. 9}$$

$$Pe' = \frac{(K_c - Y)r_p^2}{8K_d D_\infty \eta_0} \Delta P \qquad \text{Eq. 10}$$

The solute molar volumes ($V_s$) at their normal boiling point can be estimated using the group contribution methods described by Schotte.[16] With $V_s$ in hand, the bulk diffusivity ($D_\infty$) can then be calculated using the Wilke–Chang correlation.[17] The dimensionless association coefficient ($\alpha_{sv}$) for the solvent was used according to Miyabe and Isogai, whereas the solute was presumed to be nonassociating ($\alpha_s = 1$).[18]

$$D_\infty = \frac{7.4 \times 10^{-8} T \sqrt{\alpha_{sv} M_{sv}}}{\eta_0 (\alpha_s V_s)^{0.6}} \qquad \text{Eq. 11}$$

The empirical correlation provides $D_\infty$ in cm$^2$ s$^{-1}$ when $T$ is given in K, the solvent molecular weight ($M_{sv}$) in g mol$^{-1}$, $\eta_0$ in cP, and $V_s$ in cm$^3$ mol$^{-1}$. $K_c$, $K_d$, and $\varphi$ all depend on the solute-to-pore radii fraction ($\lambda$). The solute radius ($r_s$) can be obtained from the Stokes–Einstein equation, so $\lambda$ can also be calculated:

$$r_s = \frac{k_B T}{6\pi\eta_0 D_\infty} \qquad \text{Eq. 12}$$

$$\lambda = \frac{r_s}{r_p} \qquad \text{Eq. 13}$$

where $k_B$ is the Boltzmann constant ($1.38 \times 10^{-23}$ J $K^{-1}$). Consequently, $\varphi$ can easily be calculated as follows when purely steric interactions are assumed between the solute and the pore wall.

$$\phi = (1 - \lambda)^2 \qquad \text{Eq. 14}$$

$K_c$ and $K_d$ can be calculated using the empirical model developed by Bowen *et al.* for $0 < \lambda \leq 0.8$,[19] which was extended by Bandini and Vezzani to $0.8 \leq \lambda \leq 1$ for practical purposes.[20] The model presumes a fully developed flow, and it uses the center-line approximation. The model parameters are listed in Table S4.

$$K_c = (2 - \phi)(A + B\lambda + C\lambda^2 + D\lambda^3) \qquad \text{Eq. 15}$$

$$K_d = E + F\lambda + G\lambda^2 + H\lambda^3 \qquad \text{Eq. 16}$$

**Table S4**. Model parameters used to calculate the hindrance factors $K_c$ and $K_d$.

| Parameter | $0 < \lambda \leq 0.8$ | $0.8 \leq \lambda \leq 1$ |
|---|---|---|
| *A* | 1 | −6.830 |
| *B* | 0.054 | 19.348 |
| *C* | −0.988 | −12.518 |
| *D* | 0.441 | 0 |
| *E* | 1 | −0.105 |
| *F* | −2.30 | 0.318 |
| *G* | 1.154 | −0.213 |
| *H* | 0.224 | 0 |

Notably, rejection does not depend on either the membrane thickness ($\Delta x$) or pore viscosity ($\eta$) according to this set of presumptions. It is also important to highlight that knowledge of the accurate molecular structures is essential for obtaining the values of $V_s$. If one wishes to obtain continuous MWCO curves, interpolation may be used to obtain $V_s$ values for arbitrary molecular weights. In this study, the predicted MWCO curves were constructed using a hypothetical

polystyrene series consisting of ethylbenzene, 1,3-diphenylbutane, 1,3,5-triphenylhexane, etc. To obtain continuous curves, virtual molecules with a step size of 1 g $mol^{-1}$, whose molecular properties were spline-interpolated between polystyrene oligomers, were fed into the model calculations. This approach can be modified for any polymer series as needed, for example, for a polyethylene glycol series consisting of ethylene glycol, diethylene glycol, triethylene glycol, etc. (**Figure S60**).

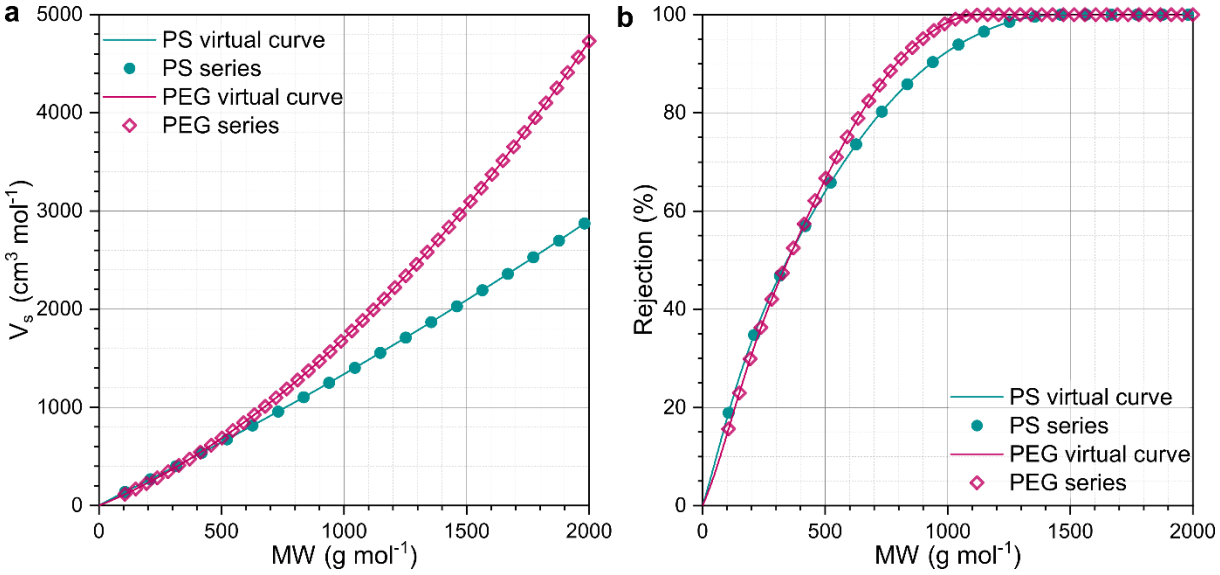


**Figure S60**. (a) Solute molar volumes ($V_s$) of polystyrene (PS) and polyethylene glycol (PEG) series obtained by the group contribution method, and continuous curves showing interpolated values. (b) Predicted discrete rejection values and continuous MWCO curves constructed using data from the PS and PEG series, and interpolated virtual values for a hypothetical isoporous membrane having a pore diameter of 2.5 nm at 30 bar and 20 °C.

The pore flow model can be extended to membranes with log-normal pore-size distribution. The key considerations and equations are described below, but the reader is referred to Bowen and Welfoot for a more detailed discussion.[21] The log-normal distribution can be described by the probability density function of the pore-size variable (r).

$$f_R(r) = \frac{1}{r\sqrt{2\pi b}} e^{-\frac{\left(\ln\frac{r}{r_p^*}+\frac{b}{2}\right)^2}{2b}} \quad \text{Eq. 17,}$$

Where,

$$b = \ln\left[1 + \left(\frac{\sigma_p^*}{r_p^*}\right)^2\right] \quad \text{Eq. 18}$$

and $r_p^*$ and $\sigma_p^*$ are the mean and the standard deviation of the pore-size distribution, respectively. The number of pores per unit area ($n(r)$) having a radius in the infinitesimal surroundings of $r$ can be obtained by the density function:

$$n(r) = f_R(r)N_0 \quad \text{Eq. 19}$$

where $N_0$ is the total number of pores per unit area. Total solute flux ($j_s$) and volumetric flux ($Q$) can be obtained by integrating their pore-wise values over the whole range of the pore-size distribution. Consequently, the overall permeate concentration can be written as the quotient of the two:

$$C_p = \frac{j_s}{Q} = \frac{\int_0^\infty N_0 f_R(r)V(r)r^2\pi C_p(r)\,\mathrm{d}r}{\int_0^\infty N_0 f_R(r)V(r)r^2\pi\,\mathrm{d}r} \quad \text{Eq. 20,}$$

where pore values are shown as a function of the pore radius. The overall rejection can be written accordingly.

$$R = \frac{\int_0^\infty \frac{f_R(r)R(r)r^4}{\eta(r)}\mathrm{d}r}{\int_0^\infty \frac{f_R(r)r^4}{\eta(r)}\mathrm{d}r} \quad \text{Eq. 21}$$

Bowen and Welfoot argued that the mathematical formula that describes the log-normal distribution may lead to results that lack physical validity.[21] The probability density of any arbitrarily large pore is low but not zero. At certain values of $r_p^*$ and $\sigma_p^*$, the presence of these large pores, which are implied by the mathematical description, can significantly affect the predicted values for rejection and other process parameters. Truncating the probability density function can bring the mathematical model closer to the physical reality. Based on experimental evidence, truncation at $r_{max} = 2r_p^*$ has been proposed.[21] Furthermore, pores smaller than the solvent molecules can be disregarded for permeation. Therefore, the $r_{min} = r_{sv}$ lower limit could be

used, where $r_{sv}$ is the radius of the solvent molecules. The corrected distribution function and the overall rejection can be written as follows.

$$f'_{\mathrm{R}}(r) = \frac{f_{\mathrm{R}}(r)}{\int_{r_{\min}}^{r_{\max}} f_{\mathrm{R}}(r)\mathrm{d}r} \qquad \text{Eq. 22}$$

$$R = \frac{\int_{r_{\min}}^{r_{\max}} \frac{f'_{\mathrm{R}}(r)R(r)r^4}{\eta(r)}\mathrm{d}r}{\int_{r_{\min}}^{r_{\max}} \frac{f'_{\mathrm{R}}(r)r^4}{\eta(r)}\mathrm{d}r} \qquad \text{Eq. 23}$$

Little experimental work has been done on solvent viscosities in nanosized channels, but a few results suggest that viscosities at the pore wall are substantially higher than viscosity values in the bulk. Based on these observations, the following correlation is proposed to calculate pore-wise average viscosities.

$$\eta(r) = \eta_0 \left[1 + 18\frac{d_{\mathrm{sv}}}{r} - 9\left(\frac{d_{\mathrm{sv}}}{r}\right)^2\right] \qquad \text{Eq. 24}$$

The diameter of the solvent molecules can be calculated from the van der Waals volumes, assuming spherical particles. The van der Waals volumes can be obtained via the group contribution method.[22]

These sets of equations can be used to predict rejection based on the isoporous pore size or on pore-size distribution. However, they can also be used to obtain pore-size information using the experimental rejection values. In this case, the model can be fitted to the experimental MWCO curve using the ordinary least-squares method.

Solvent permeance ($P$) can also be easily obtained for isoporous membranes using the Hagen–Poiseuille correlation. In the case of composite materials, the correlation is corrected using the proportion of the porous media in the selective layer ($\omega$), which is referred to as MOF coverage in this study:

$$P = \varepsilon \frac{r_{\mathrm{p}}^2}{8\eta\,\Delta x}\omega \qquad \text{Eq. 25,}$$

where $\varepsilon$ is the porosity of the selective membrane layer. The analogous equation for a membrane with a log-normal pore-size distribution could be written as follows.

$$P = \frac{N_0 \, \pi \, \omega}{8 \, \Delta x} \int_{r_{\min}}^{r_{\max}} \frac{f'_{\mathrm{R}}(r) r^4}{\eta(r)} \mathrm{d}r \qquad \text{Eq. 26}$$

$N_0$ is rarely known, but it can be obtained using the following correlation if the porosity of the selective layer is known.

$$\varepsilon = N_0 \, \pi \int_{r_{\min}}^{r_{\max}} f'_{\mathrm{R}}(r) r^2 \, \mathrm{d}r \qquad \text{Eq. 27}$$

a single equation to obtain the solvent permeance.

$$P = \frac{\varepsilon}{8 \, \Delta x} \frac{\int_{r_{\min}}^{r_{\max}} \frac{f'_{\mathrm{R}}(r) r^4}{\eta(r)} \mathrm{d}r}{\int_{r_{\min}}^{r_{\max}} f'_{\mathrm{R}}(r) r^2 \, \mathrm{d}r} \qquad \text{Eq. 28}$$

For the isoporous membrane predictions, the porosity was calculated using the estimated pore size and density obtained from crystallographic data. For the membrane predictions corrected for pore distribution, $N_0$ was assumed to be identical to the value in the isoporous scenario.

To estimate the solvent permeance through a heteropore Kagome topology in ETTA structure, the pore flow model as detailed above is modified by considering the ratio of the permeance through the large and small pores.

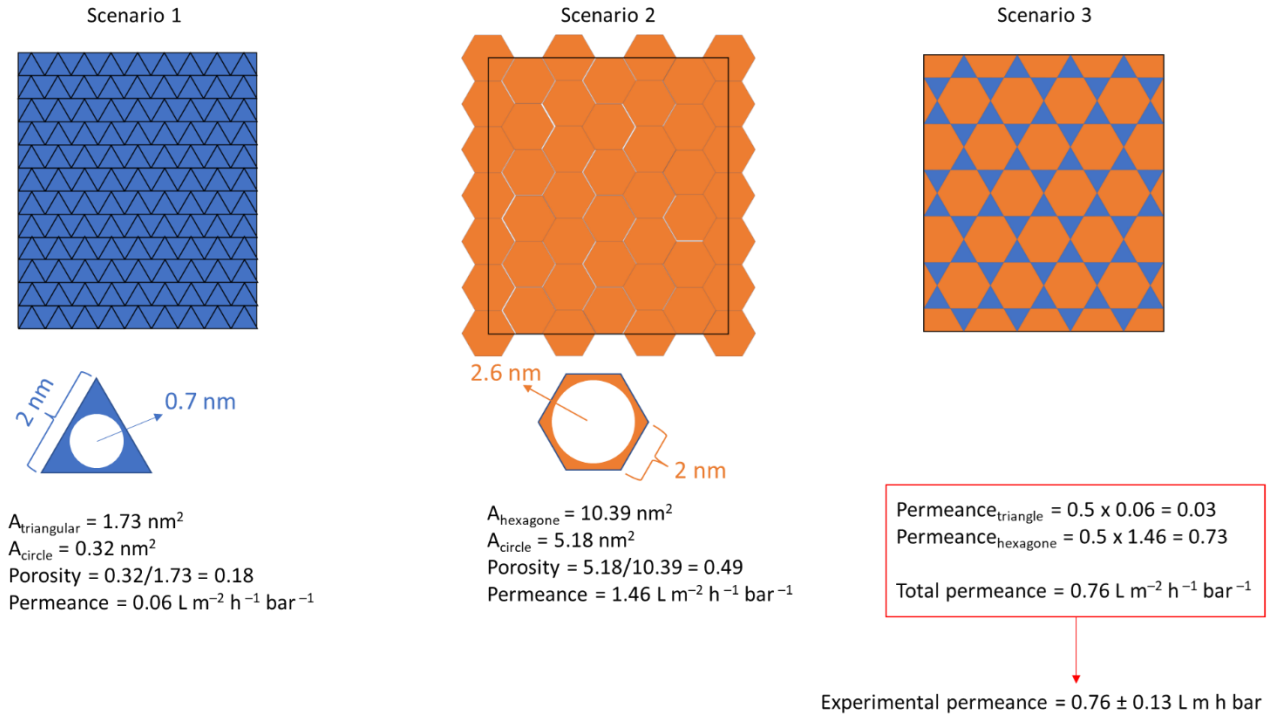


**Figure S61.** Theoretical model of homopores comprise completely triangular (scenario 1) and completely hexagonal (scenario 2) shapes, and heteropore comprises triangular and hexagonal shapes.

## *3.2 Experimental OSN Results*

**Table S5**. Solvent flux at various pressure.

| Pressure (bar) | toluene | | acetonitrile | | methanol | | acetone | |
|---|---|---|---|---|---|---|---|---|
| | Flux (L $m^{-2}$ $h^{-1}$) | std. dev | Flux (L $m^{-2}$ $h^{-1}$) | std. dev | Flux (L $m^{-2}$ $h^{-1}$) | std. dev | Flux (L $m^{-2}$ $h^{-1}$) | std. dev |
| 1 | 2.88 | 1.05 | 4.32 | 0.66 | 4.65 | 0.65 | 8.28 | 1.44 |
| 5 | 14.87 | 3.71 | 20.43 | 2.67 | 20.90 | 4.82 | 38.09 | 8.80 |
| 10 | 32.04 | 6.63 | 48.23 | 8.25 | 48.86 | 4.64 | 82.02 | 10.99 |
| 15 | 56.63 | 8.87 | 80.84 | 8.11 | 83.65 | 7.93 | 107.26 | 10.34 |
| 20 | 70.33 | 12.88 | 110.07 | 14.02 | 114.80 | 15.97 | 148.14 | 11.61 |
| 30 | 116.55 | 12.79 | 157.54 | 15.74 | 162.86 | 20.03 | 231.32 | 13.80 |

**Table S6**. Rejection values of various solutes by TZ–Tf film in acetone at 20 °C and 30 bar

| Solutes | Molecular weight (g $mol^{-1}$) | Rejection (%) | std. dev |
|---|---|---|---|
| Styrene dimer | 236.35 | 25.33 | 2.37 |
| Methyl orange | 327.33 | 24.74 | 4.78 |
| Losartan | 422.92 | 33.69 | 3.39 |
| 4CzIPN | 788.89 | 65.63 | 3.93 |
| Roxithromycin | 837.06 | 72.84 | 3.56 |
| Rose bengal | 973.67 | 74.01 | 1.97 |
| CAS 870987-63-6 | 1121.91 | 78.77 | 3.24 |
| CAS 75777-87-6 | 1196.19 | 84.25 | 5.40 |
| SA 667250 | 1921.32 | 97.80 | 1.89 |

**Table S7**. Rejection values of various solutes by TZ–Tf film in acetonitrile at 20 °C and 30 bar

| Solutes | Molecular weight (g $mol^{-1}$) | Rejection (%) | std. dev |
|---|---|---|---|
| Styrene dimer | 236.35 | 19.42 | 4.20 |
| Methyl orange | 327.33 | 39.84 | 6.40 |
| Losartan | 422.92 | 44.43 | 3.20 |
| 4CzIPN | 788.89 | 74.85 | 4.94 |
| Roxithromycin | 837.06 | 85.58 | 4.79 |
| Rose bengal | 973.67 | 86.64 | 3.38 |
| CAS 870987-63-6 | 1121.91 | 91.59 | 1.66 |
| CAS 75777-87-6 | 1196.19 | 93.08 | 4.27 |
| SA 667250 | 1921.32 | 98.82 | 0.66 |

**Table S8**. Rejection values of various solutes by TZ–Tf film in methanol at 20 °C and 30 bar

| Solutes | Molecular weight (g $mol^{-1}$) | Rejection (%) | std. dev |
|---|---|---|---|
| Styrene dimer | 236.35 | 31.76 | 3.69 |
| Methyl orange | 327.33 | 42.33 | 5.37 |
| Losartan | 422.92 | 53.36 | 3.22 |
| Roxithromycin | 837.06 | 95.39 | 2.34 |
| Rose bengal | 973.67 | 92.01 | 2.65 |
| CAS 870987-63-6 | 1121.91 | 94.29 | 2.84 |
| CAS 75777-87-6 | 1196.19 | 97.17 | 1.81 |
| SA 667250 | 1921.32 | 98.61 | 1.39 |

**Table S9**. Rejection values of various solutes by TZ–Tf film in toluene at 20 °C and 30 bar

| Solute | Molecular weight (g mol$^{-1}$) | Rejection (%) | std. dev |
|---|---|---|---|
| Styrene dimer | 236.35 | 16.56 | 2.34 |
| Isodrine | 364.91 | 21.32 | 2.55 |
| Hexaphenylbenzene | 534.69 | 34.92 | 2.35 |
| Rhodanile Blue | 778.38 | 58.66 | 2.64 |
| Ir(tBuppy)3 | 826.12 | 64.80 | 3.73 |

**Table S10**. Rejection values of various solutes by ETTA–Tf film in toluene at 20 °C and 30 bar

| Solute | Molecular weight (g mol$^{-1}$) | Rejection (%) | std. dev |
|---|---|---|---|
| Styrene dimer | 236.35 | 22.74 | 3.66 |
| Isodrine | 364.91 | 25.09 | 5.41 |
| Hexaphenylbenzene | 534.69 | 40.38 | 6.89 |
| Rhodanile Blue | 778.38 | 60.54 | 7.32 |
| Ir(tBuppy)3 | 826.12 | 59.04 | 4.89 |

**Table S11**. Rejection values of various solutes by TAPA–Tf film in toluene at 20 °C and 30 bar

| Solute | Molecular weight (g mol$^{-1}$) | Rejection (%) | std. dev |
|---|---|---|---|
| Styrene dimer | 236.35 | 16.46 | 1.69 |
| Isodrine | 364.91 | 22.04 | 2.20 |
| Hexaphenylbenzene | 534.69 | 32.42 | 3.20 |
| Rhodanile Blue | 778.38 | 56.01 | 2.39 |
| Ir(tBuppy)3 | 826.12 | 64.06 | 2.23 |

**Table S12**. Rejection values of various solutes by TAPB–Tf film in toluene at 20 °C and 30 bar

| Solute | Molecular weight (g mol$^{-1}$) | Rejection (%) | std. dev |
|---|---|---|---|
| Styrene dimer | 236.35 | 17.64 | 1.63 |
| Isodrine | 364.91 | 23.60 | 1.68 |
| Hexaphenylbenzene | 534.69 | 36.29 | 2.41 |
| Rhodanile Blue | 778.38 | 56.97 | 3.23 |
| Ir(tBuppy)3 | 826.12 | 58.90 | 3.51 |

**Table S13**. Toluene permeance values of various films at 20 °C and 30 bar

| Films | Permeance ($L\ m^{-2}\ h^{-1}\ bar^{-1}$) | std. dev |
|---|---|---|
| TAPA–Tf | 2.37 | 0.28 |
| TZ–Tf | 3.91 | 0.32 |
| ETTA–Tf | 0.76 | 0.13 |
| TAPB–Tf | 2.59 | 0.28 |

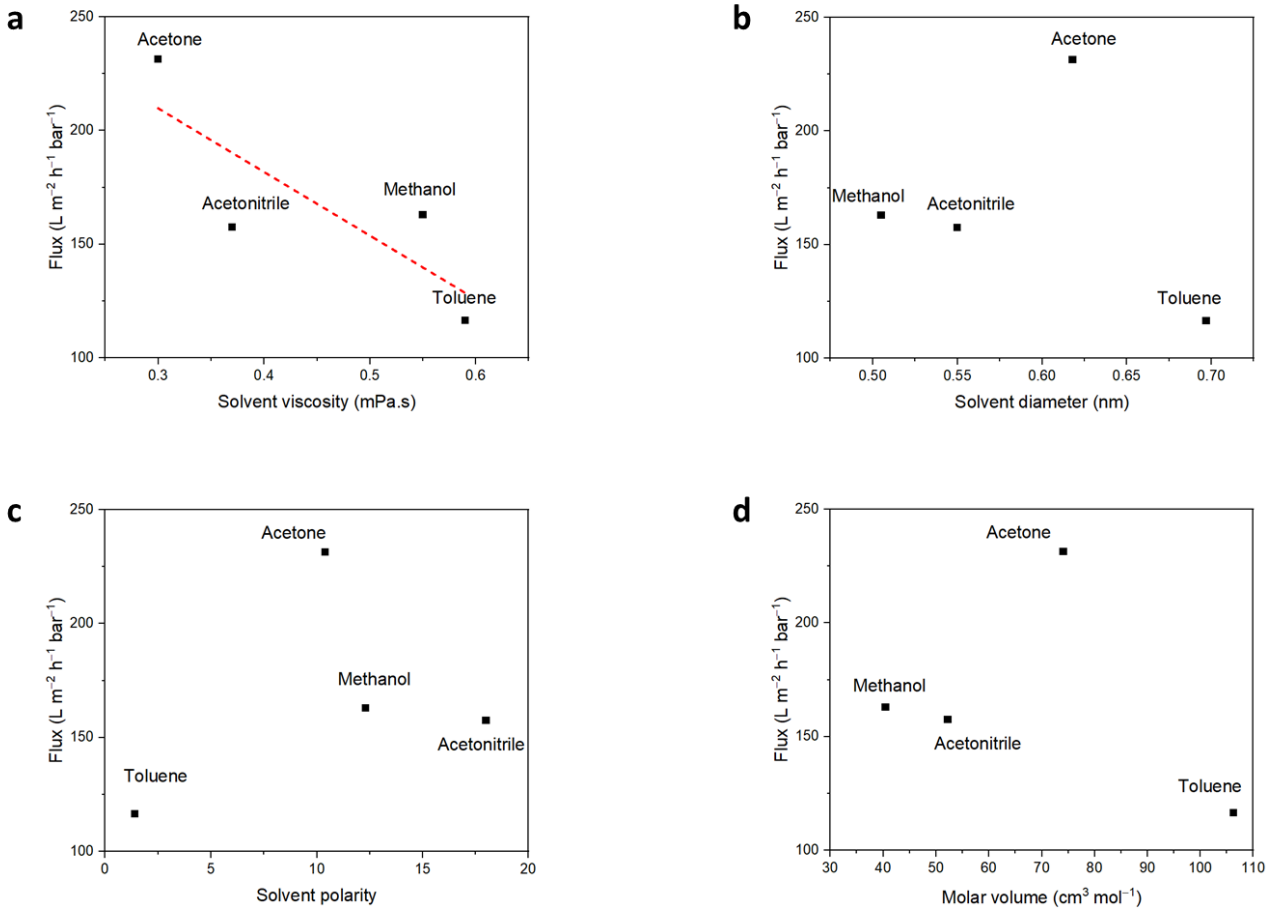


**Figure S62**. Correlations between solvent flux with solvent viscosity (a), molecular diameter (b), polarity (c), and molar volume (d).

# References


[1] J. Gayle, S. Roy, S. Gupta, S. Hassan, A. Rao, P. G. Demingos, K. Miller, G. Guo, X. Wang, A. Garg, C. V. Singh, R. Vajtai, J. T. Robinson, P. M. Ajayan, *ACS Appl. Mater. Interfaces* **2024**, *16*, 2726.

[2] R. Xia, H. Zhou, Z. Zhang, R. Wu, W.-P. Wu, *Polymer Engineering & Science* **2018**, *58*, 2071.

[3] K. A. Miller, L. B. Alemany, S. Roy, Q. Yan, P. G. Demingos, C. V. Singh, S. Alahakoon, E. Egap, E. L. Thomas, P. M. Ajayan, *ACS Appl. Mater. Interfaces* **2022**, DOI 10.1021/acsami.1c17501.

[4] Y. Zhu, H. Wang, J. Zhu, L. Chang, L. Ye, *Applied Surface Science* **2015**, *349*, 27.

[5] T. Roopa, H. N. Murthy, D. Harish, A. Jain, G. Angadi, *Polymers and Polymer Composites* **2021**, *29*, 198.

[6] M. L. B. Palacio, Y. Wang, W. W. Gerberich, *J. Mater. Res.* **2001**, *16*, 3628.

[7] S. Hur, S. I. Hong, D. K. Shin, *KEM* **2005**, *297–300*, 237.

[8] C. A. Charitidis, E. P. Koumoulos, V. Nikolakis, D. A. Dragatogiannis, *Thin Solid Films* **2012**, *526*, 168.

[9] J. C. Tan, T. D. Bennett, A. K. Cheetham, *Proceedings of the National Academy of Sciences* **2010**, *107*, 9938.

[10] D. N. Awang Chee, F. Aziz, M. A. Mohamed Amin, A. F. Ismail, *emergent mater.* **2022**, *5*, 1289.

[11] Y. Zhang, C. Pan, *Diamond and Related Materials* **2012**, *24*, 1.

[12] S. Mukherjee, Z. Zeng, M. M. Shirolkar, P. Samanta, A. K. Chaudhari, J.-C. Tan, S. K. Ghosh, *Chemistry – A European Journal* **2018**, *24*, 11771.

[13] W. R. Bowen, J. S. Welfoot, *Chemical Engineering Science* **2002**, *57*, 1121.

[14] P. Silva, A. G. Livingston, *Journal of Membrane Science* **2006**, *280*, 889.

[15] J. L. C. Santos, P. de Beukelaar, I. F. J. Vankelecom, S. Velizarov, J. G. Crespo, *Separation and Purification Technology* **2006**, *50*, 122.

[16] W. Schotte, *The Chemical Engineering Journal* **1992**, *48*, 167.

[17] C. R. Wilke, P. Chang, *AIChE Journal* **1955**, *1*, 264.

[18] K. Miyabe, R. Isogai, *Journal of Chromatography A* **2011**, *1218*, 6639.

[19] W. R. Bowen, A. W. Mohammad, N. Hilal, *Journal of Membrane Science* **1997**, *126*, 91.

[20] S. Bandini, D. Vezzani, *Chemical Engineering Science* **2003**, *58*, 3303.

[21] W. R. Bowen, J. S. Welfoot, *Chemical Engineering Science* **2002**, *57*, 1393.

[22] A. Bondi, *The Journal of Physical Chemistry* **1964**, *68*, 441.